NTNU
Norwegian University of
Science and Technology

Growth of Fatigue Cracks in Mooring Line Chains

Martin Hove

Mechanical Engineering
Submission date: June 2016
Supervisor: Per Jahn Haagensen, KT
Co-supervisor: Jochen Köhler, KT

Norwegian University of Science and Technology
Department of Structural Engineering

Preface

This study is the result of the work performed as part a master thesis written for the Department of Structural Engineering (KT) at the Norwegian University of Science and Technology (NTNU), and is the continuation of a literature study performed in the fall of 2015. The study is part of a larger project to investigate the fatigue life of offshore mooring chains based on their surface condition.

This thesis focuses on numerical calculations of stress intensity factors of cracks performed in ABAQUS. In order to have a good understanding of the system, an introduction to mooring systems and offshore structures have been included, as well as a summary of the state of the art in both fatigue and fracture mechanics calculations in the industry today. The target group for this study is engineers working with offshore structures, or individuals which have an interest in the use of fracture mechanics with fatigue.

I would like to thank my supervisors at NTNU, Per Jahn Haagensen and Jochen Köhler for their guidance and advice. I would further like to thank Kristin Hanem Tømmervåg and Alexander Hoel for their efforts with our combined work, and Sunny Islam for always being open for questions on fracture mechanics.

Last but not least, I would like to thank my parents for their continous support throughout my years of study.

Abstract

This master thesis is the continuation of a project work conducted during the fall of 2015, and is part of a series of studies investigating the effect of surface condition on the fatigue life of mooring chains. The study focuses on the use of fracture mechanics to predict the fatigue life of a mooring chain with a corrosion pit. In order to do this, a fatigue model was proposed which is divided into a local and a global model. The local model considers the surface of the chain link by modelling a 20mm segment of the surface at the crown of the chain link as a plate with a corrosion pit. The pit was idealized as a hemispherical notch of radius 1mm. The finite element method was used to model cracks initiating at different locations in the corrosion pit.

Three hypotheses were suggested for the crack initiation and growth. The first hypothesis assumes that the crack starts in the bottom of the pit, and grows with a circular crack front, until it encompasses the whole pit. After the pit is encompassed, it continues growing first as a circular crack and then the crack front changes into an elliptic shape. The second hypothesis assumes that the crack starts on the surface of the plate, in the side of the notch, and that the crack continues growing until it reaches the same depth as the corrosion pit. It will then grow into an elliptic crack of crack ratio 0.5, encompassing the pit, with origin at the original crack origin. The third hypothesis assumes that the crack initially encompasses the pit, and grows as a circular crack until the crack front changes shape into an elliptical front.

The first part of the crack growth is modelled in the local model. This was done by writing a python script for ABAQUS, which would calculate the stress intensity factor of the crack, and then move the crack front incrementally and remesh the model as the crack progressed. The results from the local model showed the expected trend, as the first and third hypotheses converged towards the handbook solution for a plate with a circular crack, while the second hypotheses converged towards the solution for a plate with an elliptical crack of ratio 0.5. It was found that the stress intensity factor for the crack originating in the side of the pit was higher than for the cracks emitting in the bottom and encompassing the pit for both tension and bending. The Kondo criteria was used to argue for the cracks being more likely to initiate in the side of the pit.

The stable crack growth was modelled in the global model, also by the use of a python script to incrementally move the crack. Three models were created. The first had a crack with a constant circular crack front shape. The second started with an initial crack ratio of 0.5 which was changed as the crack progressed. The same was done for the third model, but with an initial crack ratio of 1.0. The stress intensity factors for the global model showed good consistency with handbook solutions.

The transition region was not modelled, and it was estimated by curve fitting the results between the local and the global model. This worked well for the first and third hypotheses. There was a discrepancy between the local and global solution for the second hypothesis, as the elliptical crack is more severe in a rod, than an equivalent crack in a plate. This caused the solutions to not align well. The discrepancy was solved by ignoring all analysis results from the local model which showed lower values for the stress intensity factor than the global model.

A MATLAB script was used to integrate Paris' law to find life estimates for the chain links for the different hypotheses. It was found that between 18 to 53% of the life of the chain link was spent in the local and transition phase, defined as a a crack depth between 0.2 to 5mm. The initial crack depth and loads were varied in order to generate a set of SN data. The data set showed a good consistency with the DNV GL SN curve for studless chain links.

Two simplified methods to calculate the stress intensity factor for a crack in the crown of the chain were reviewed. They showed non-conservative results with an error of about 10% in the early growth phase. Due to these attributes, they are not recommended for further use.

It is recommended to perform more studies on the effect of different pit geometries. More research should also be done in order to find how the crack front shape develops from cracks originating at different locations in the pit.

Sammendrag

Denne masteroppgaven er fortsettelsen på et prosjekt som ble skrevet på høsten 2015, og er del av en serie av oppgaver som undersøker effekten overflatetilstanden til en kjetting har på dens levetid. Dette studiet fokuserer på bruken av bruddmekanikk til å predikere levetiden til en kjetting med korrosjongroper. For å gjøre dette ble det foreslått en utmattingsmodell som er delt i to deler; en lokal og en global model. Den lokale modellen modellerer et 20mm segment av overflaten til kronen på kjettingen som en plate med en korrosjon grop. Gropen er idealisert som en halvsirkulær kjerv med radius på 1mm. Elementmetoden ble brukt til å modellere sprekker voksende i gropen.

Det ble foreslått tre hypoteser for initiell sprekkplassering og hvordan den siden vokser gjennom kronen til kjettingen. Den første hypotesen antar at en sirkulær overflatesprekk starter i bunnen av gropen, og at den vokser til den dekker hele gropen. Etter dette vokser den med en sirkulær sprekkfront som etterhvert utvikler seg til å bli elliptisk. Den andre hypotesen antar at sprekken starter i hjørnet av gropen ved overflaten, og at den vokser med en sirkulær front til den er like dyp som gropen. Etter dette vokser den til den har en elliptisk front, med en ratio på 0.5 som går rundt hele gropen. Den tredje hypotesen antar at sprekken til å begynne med dekker hele gropen, og at den fortsetter å vokse med en sirkulær front til den begynner å utvikle seg til en elliptisk sprekk.

Den første delen av sprekkveksten er modellert i den lokale modellen. Dette ble gjort ved å skrive et python script til ABAQUS, som ville beregne spenningsintensitetsfaktoren til sprekken, også flytte sprekken inkrementsvis dypere. Når sprekken ble flyttet, ble det laget et nytt mesh, og en ny beregning utført. Resultatene fra den lokale modellen viste samme trend som var forventet hvis hypotesen stemte, ettersom sprekkene fra hypotese en og to konvergerte mot håndbokløsningen for en sirkulær sprekk i en plate, mens sprekken fra hypotese to konvergerte mot håndbokløsningen for en elliptisk sprekk. Den stabile sprekkveksten ble modellert i den globale modellen. Her ble det også brukt et python script for å flytte sprekken fremover, remeshe, og beregne spenningsintensitetsfaktor for den nye sprekkdybden. Tre modeller ble laget. Den første hadde en sprekk som hadde en konstant sirkulær sprekk front for hele veksten. Den andre startet med en sprekk ratio på 0.5, som så endret seg etterhvert som sprekken vokste. Den tredje modellen hadde også en endrende sprekk front, men begynte med en ratio på 1.0. Spenningsintensitetsfaktorene fra den globale modellen stemte godt med håndbokløsninger.

Overgangsregionen ble ikke modellert, men estimert ved å tilpasse kurver til de lokale og globale resultatene samlet. Dette fungerte bra for den første og tredje hypotesen. Det oppstod et problem for den andre hypotesen, ettersom den brukte en elliptisk sprekkform. En elliptisk sprekk har en høyere spenningsintensitetsfaktor relativt til en sirkulær sprekk for staver enn for plater. Dette medførte at resultatene for den lokale modellen for sprekken som startet i siden var lavere enn forventet. Ved å ignorere datapunktene i den lokale modellen som lå under den globale modellen når kurvetilpasningen ble utført, ble det funnet et konservativt estimat til sprekkveksten.

Et MATLAB script ble brukt til å integrere Paris' lov for å finne estimeterte levetider for kjettingløkker ved de forskjellige hypotesene. Andelen av livet til kjettingen som ble tilbragt med en sprekkdybde mellom 0.2 og 5mm, lå på mellom 18 og 53% av den totale levetiden. Forskjellige initielle sprekkdybder og laster ble brukt for å lage spenning-liv datasett. Disse settene viste en god sammenheng med spenning-livs kurvene til DNV GL som blir brukt for kjettingløkker uten tverrpinner.

To forenklede metoder for å beregne spenningsintensitetsfaktoren for en sprekk i kronen av kjettingen ble undersøkt. De viste ikke-konservative resultater, og en feil på rundt 7% for en sprekkdybde mindre enn 0.3(a/D). Faktumet at løsningene var ikke konservative er en lite ettertraktet egenskap, og de anbefales derfor ikke for videre bruk.

Det anbefales å gjøre videre studier på effekten av forskjellige geometrier på korrosjonsgropene. Det burde også gjøres flere analyser for å finne ut nøyaktig hvordan sprekkfronten utvikler seg når den vokser fra sprekker de forskjellige stedene i gropene.

Nomenclature

$\bar{a}_f$	Effective final flaw parameter.
$\bar{a}_i$	Effective initial flaw parameter.
$\bar{a}$	Effective flaw parameter.
$\Delta\bar{K}$	Equivalent stress intensity range.
$\Delta\sigma$	Stress Range.
ΔK	Stress intensity factor range.
ΔK_{op}	Stress intensity at crack opening.
ΔK_{th}	Stress intensity threshold.
γ	Walker curve fitting parameter.
σ_a	Stress amplitude.
σ_m	Mean cyclical stress.
σ_{ar}	Fully-reversible stress amplitude.
σ_{ij}	Stress Tensor.
σ_{max}	Maximum cyclical stress.
a_f	Final crack length.
a_i	Initial crack length.
a_s	Crack depth as measured from surface of component.
K_c	Fracture toughness of material.
K_I	Stress intensity factor for mode one loading.
K_{eff}	Efficient stress intensity.
K_{max}	Maximum stress intensity factor.
N_f	Number of cycles until failure.
C	Crack growth parameter.
D_C	Design Capacity
D_L	Design Load Effect
F	Geometry function.
F_b	Geometry function for bending.
F_T	Total geometry function.
F_t	Geometry function for tension.

m	Crack growth parameter.
R	Stress intensity ratio.
S	Nominal stress.

Acronyms

BSI	British Standard Institution.
DOF	Degree of Freedom.
DP	Dynamic Positioning System.
FPSO	Floating Production, Storage and Offloading unit.
H1	Hypothesis 1.
H2	Hypothesis 2.
H2M	Modified Hypothesis 2.
H3	Hypothesis 3.
JIP	Joint Industry Project.
MIC	Microbiologically Influenced Corrosion.
OPB	Out of Plane Bending.
SCC	Stress Corrosion Cracking.
SCF	Stress Concentration Factor.
SIF	Stress Intensity Factor.
SM	Spread Moored System.
SN	Stress Life .
SPM	Single Point Mooring System.
SSCC	Sulphide Stress Corrosion Cracking.

Contents

Chapter 1

Introduction

When conducting marine operations offshore, the capability to reliably remain at a specific location is of utmost importance. For production units, the loss of position may result in the rupture of risers, or at worst, the loss of human life. Mooring systems have therefore been developed in order to ensure that the vessels remain stationary. These systems consists of different components, such as wire ropes and chains. The high resistance against wear and mechanical loading make the chain a crucial component at regions of high wear, such as the trash zone (the sea bed) and splash zone (sea level).

The failure of mooring lines can be extremely costly, as seen with the Gryphon Alpha incident, which had an approximated insurance cost of 440 million £ as the risers ruptured due to loss of position in a storm [Crighton]. It is therefore imperative to be able to predict the life of the mooring lines, in order to have them replaced before the risk of failure becomes too great. The degrading mechanisms on mooring chains are so far not well understood, and an accurate a priori estimate of life is therefore not available. In order to ensure safe operation, the lines are subject to inspections at regular intervals during their service life. There are as of today no clear criteria for deciding whether a chain is too damaged to continue service or not.

1.1 Joint Project

> *The master's thesis work presented in this report is part of a collaborative project involving Statoil ASA and the Department of Structural Engineering at the Norwegian University of Science and Technology (NTNU). The final objective is to provide Statoil with tools for assessing surface conditions on mooring chain links in order to evaluate the remaining service life of the entire mooring line. Chain lengths, which have been in service on floating offshore structures for approximately 15 years, have been retrieved by Statoil to be studied at NTNU. Full scale fatigue testing is currently in process, where lengths of three chain links are subjected to cyclic tensile loading in a corrosive environment. The corrosion fatigue testing will provide the remaining lives of the lengths tested. At the time of writing, three master students, including the author, are involved in the joint project. Different topics are covered by the resulting theses. In order to obtain best possible understanding of the field of research and the progression of the joint project, the reader is referred to the theses of Kristin Hanem Tømmervåg and Alexander Hoel, to be published within summer of 2016, as well as a previous master thesis by Bjørnsen (2014). The reader should also be aware that a doctorate study and further master thesis studies currently are under development at the Department of Structural Engineering at NTNU.*

- Alexander Hoel, Kristin Hanem Tømmervåg and Martin Hove

1.2 Objective of Study

The goal of this study is to investigate the fatigue life of a mooring chains, and their remaining lives based on their surface condition. The focus of this study will be on the effect of corrosion pits on fatigue life, and the crack growth through the crown of a chain link. The study has the following objectives:

- Present the current methods for calculating fatigue life of mooring chains.
- Evaluate the effect of having a crack initiate at different locations in a corrosion pit.
- Estimate the fatigue life of a mooring chain link with a corrosion pit through the use of fracture mechanics.

As the study progressed, the need for a simplified fracture mechanics analysis method for the chain link was identified. Therefore, a simplified method proposed in the literature was evaluated, as well as an alternative method proposed by the author. The review of the methods is presented in Appendix A.

1.3 Scope of Study

As the study is part of a larger project, the effects of corrosion and investigations of corrosion pit geometries will not be included. If this is of interest, the reader is referred to the theses by Kristin Hanem Tømmervåg and Alexander Hoel which will become available by the summer 2016. The thesis futher limits itself to:

- Idealized corrosion pits.
- A crack initiating in the crown of the chain link.
- The use of predetermined crack propagation paths.
- The tensile loading case on the chain links.

Chapter 2

Offshore Installations and Mooring Systems

2.1 Introduction to Offshore Installations

Offshore structures are being used by the oil and gas industry all over the world, and have been in active service on the Norwegian continental shelf since 1971. There are mainly two different types of systems; fixed and floating structures [Keshavarz, 2011]. Fixed structures are costly, and their installation is challenging for deeper waters [Bjørnsen, 2014, p.39].The floating production systems have appeared as a cheap and secure alternative. Figure 2.1 shows five different offshore structure configurations, all of which are in use today.

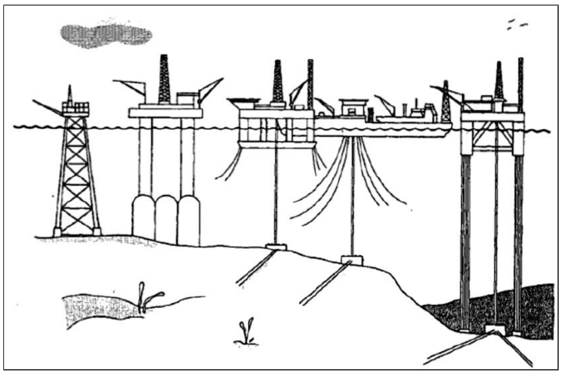

Figure 2.1: Five different offshore structures from left to right; two types of fixed structures, a semi-submersible platform, a floating production unit and a tension leg platform. [Bjørnsen, 2014, p.39]

A mooring system is put in place in order to keep the production unit or offshore structure stationary within a given tolerance. The system must withstand the environmental loads it will be subjected to, which consist mostly of wave and wind loads. Different floating structures have different of degrees of freedom (Degree of Freedom (DOF)s). If they are neutrally buoyant, the structures will have six DOFs as seen in Figure 2.2. A tension leg platform is positively buoyant and fastened to the sea bed, which results in permanent tension in it's mooring lines. It is therefore restrained in the heave, pitch and roll directions [Keshavarz, 2011, p.3], resulting in only three DOFs.

A Floating Production, Storage and Offloading unit (Floating Production, Storage and Offloading unit (FPSO)) is a floating vessel used by the offshore industry for the processing and storage

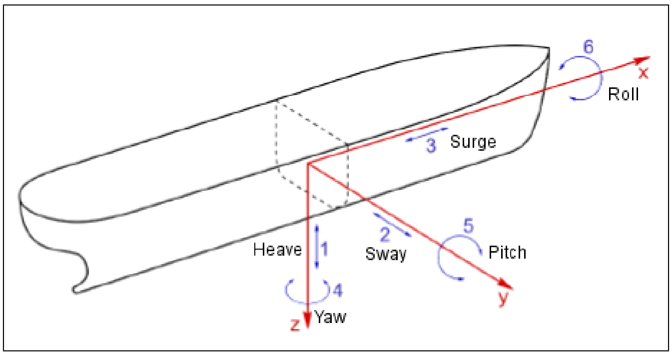

Figure 2.2: Degrees of Freedom for neutrally buoyant structure, [Bjørnsen, 2014, p. 56].

of oil and gas. They are usually ship-shaped structures, held in place by a different types of mooring systems, depending on the environmental conditions where the FPSO will operate. FPSOs are widely used in deeper waters, where piping and construction of fixed structures is expensive. They are also frequently used for smaller oil fields with shorter operational life times.

Semi-submersible platforms are stable, and have good sea-keeping characteristics [Keshavarz, 2011, p.4]. Their main area of operation are as drilling rigs, oil production platforms and heavy lift cranes. These platforms are multi-legged structures with a large deck, that connect to pontoons underwater. They are relatively easy to move, and the buoyancy of the platform can be adjusted through the pontoon. This allows for the platform to be used at different water depths.

SPARs are deepwater drilling and production platforms, and have been designed in three different configurations; cylindrical hull, truss and cell spar. The basic principle of a SPAR is to have a large portion of the structure submerged vertically below the platform, with some sort of ballast at the bottom, and buoyancy chambers near the surface, in order to make the structure more stable. The SPAR is moored to the sea bed by mooring lines attached to the submerged structure [Keshavarz, 2011, p.5].

Tension leg platforms are moored tightly and vertically by taut mooring lines, called tendons or tethers. As mentioned previously, this mooring configuration results in the reduction from six to three DOFs of motion.

2.2 Mooring Systems

There are many different variants of mooring systems, with varying components, as well as installation configuration. The requirements for these systems vary with the conditions, as well as the projected mooring period. DNV operates with three different mooring system categories, for typical units as seen in Table 2.1, [DNV-OS-H203, p.21].

Table 2.1: Mooring periods, and typical units.

	Long-Term/Permanent	**Mobile Mooring**	**Weather Restricted Mooring**
Mooring Period	> 5 Years	< 5 Years	Operation reference period
Typical Unit	Production Vessel, Storage Unit,Loading Buoy	Drilling Vessel,Accomodation Unit	Vessels involved in in Marine Operations Offloading/Berthing

The two most commonly used mooring system configurations are Spread Moored (SM) - and

Single Point Mooring (SPM) systems [Europe, 2006, p.21]. A spread mooring system will ensure that the structure remains in the same direction, without weather-vaning. These systems are mostly used in areas with little and uniform weather, due to their simplicity. In areas with stronger and more irregular weather, like the North Sea, the use of SPM is widespread. SPM allows the structure to face the weather in the direction of least resistance, thus reducing the total load on the mooring system [Hoel et al., 2015, p.14]

As an addition to the passive mooring systems, dynamic positioning systems have been introduced. These system allow the vessel to turn and move, thus reducing offset of position. This lowers the load on the system, much like the SPM. The following sections will introduce different components of mooring systems, and also discuss some of the fundamental features of such a system, starting from the surface of the sea and moving down to the seabed along the mooring line.

2.2.1 Turret Mooring Systems

Turret systems consist of a turret assembly that is fastened onto or integrated into the vessel, and then permanently moored to the seabed. It contains bearing systems, which allows the vessel to rotate while the turret system remains at the same location. There are two main configurations; internal and external turrets. In an internal turret system, the turret is integrated into the hull of the system. In comparison, the external turret system is attached to the vessel, usually the bow. There are variants of the external system, which allow for the turret to be disconnected during service. If disconnected, the turret remains floating through the assistance of a buoy, and can be reconnected at a later time. [Blue Water, a]

(a) Internal Turret Mooring System. [Blue Water, b]

(b) External Turret Mooring System. [Blue Water, c]

Figure 2.3: Turret types.

The end part of the turrets use either trumpets or fairlead systems to guide and control the mooring lines. Fairleads can rotate around their own axis, which reduces the bending momentum in the upper regions of the chain.

Trumpets perform the same function as fairleads, but are usually stationary tubes which the chains go through. They are used in both internal and external turret systems. As the chains are sliding through the trumpet, friction and excessive wear is considered a major challenge, and has been studied in different joint industry projects (JIPs) [Brown et al., 2005, p.5].

2.2.2 Dynamic Positioning System and Active Winching

Dynamic Positioning Systems (Dynamic Positioning System (DP)) can be found in all kinds of vessels used by the offshore industry. It's function is to maintain the position of the vessel, which it does by measuring the current heading and position and comparing it to a reference.

Adjustments are then made by using the thrusters on the ship. DPs can be used with vessels that are moored, or not moored. [Keshavarz, 2011, p.10]

A second system used only for ships that are moored, is active winching. It works by continuously measuring the tension in the mooring lines, and adjusting it to obtain the optimal tension for use. In addition, the active winching allows the operator to change which links that are subject to the largest amount of wear. As an example, the chain link at the end of the trumpet is often subject to extra degradation due to wear and new material being exposed to corrosion. In such cases, the active winching system can loosen or tighten the lines in order to ensure that each individual chain does not remain at the most damaging locations for excessive periods of time. [Keshavarz, 2011, p.10]

2.2.3 Line Configurations

The mooring lines can be configured in three different ways:

- Catenary mooring
- Taut mooring
- Tension leg mooring

The catenary configuration, as seen in Figure 2.4a consists of multiple mooring lines, attached to the floating structure and an anchor at the sea bed. A large amount of chain is located at the seabed, and the restoring forces in this configuration come from weight of the line, as well as frictional forces at the seabed. Catenary lines are mostly used in shallow waters, as they require a large amount of chain at the seabed in order to be effective. Having large amounts of chain at the seabed increase the risk of mooring lines clashing with each other, pipelines or subsea equipment [Keshavarz, 2011, p. 8], which is not desirable. The lines are usually made of different components, with the lower section being made of chain, and the upper section of fiber ropes.

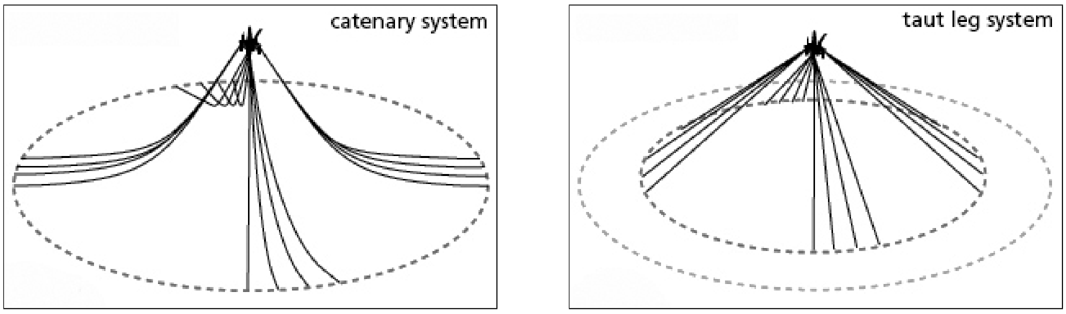

(a) http://www.dredgingengineering.com/moorings/overview/Tool%20Ibb.html *(b) http://www.dredgingengineering.com/moorings/overview/Tool%20Ibb.html*

Figure 2.4: Line configurations.

The taut configuration is used for deeper waters, where the weight of the mooring line becomes a limiting factor. It consists of multiple lines, connected to the structure from the sea bed with taut lines, usually at an angle of 30-45 degrees to horizontal at the vessel. The elasticity of the mooring lines need to be high enough that the motion of the structure can be absorbed without causing overload. The taut mooring lines require less seabed area.

The tension leg configuration consists of a set of legs or tendons that attach the platform to a template or foundation on the seafloor. It is subject to a positive buoyancy, and equilibrium is achieved by keeping the legs in constant tension. As discussed earlier in Section 2.1, this configuration results in the reduction from six to three DOFs (surge, sway and yaw).

2.2.4 Line Components

Mooring lines consist of connectors at each end, and different components. Some examples of components are chains, wire- and fiber ropes.

Chains

The chains that are currently being tested in the laboratory, are produced by the Swedish company Ramnäs Bruk and the spanish company Vicinay Cadenas S.A. The production method for chains are comprehensive, and Ramnäs' method will be described in the current section.

Before starting the production procedure, the raw material of steel rolled bars, is inspected. Afterwards they are cut into unit sized lengths, called blanks. These blanks are then heated by electrical resistance heaters, and bent into the shape of a chain link, in such a way that the two ends are positioned opposite each other, but not in contact. The ends are then welded together by flash-butt welding. In this process, external current is applied to the two ends of he chain, and the arc that is generated between the two ends will heat the material. The two ends are then fused by pressing them together [SubsTech]. The impurities in the base metal will be forced out, and the weld is planed in order to fit the dimensional criteria set by the standard [Bjørnsen, 2014, p.10].

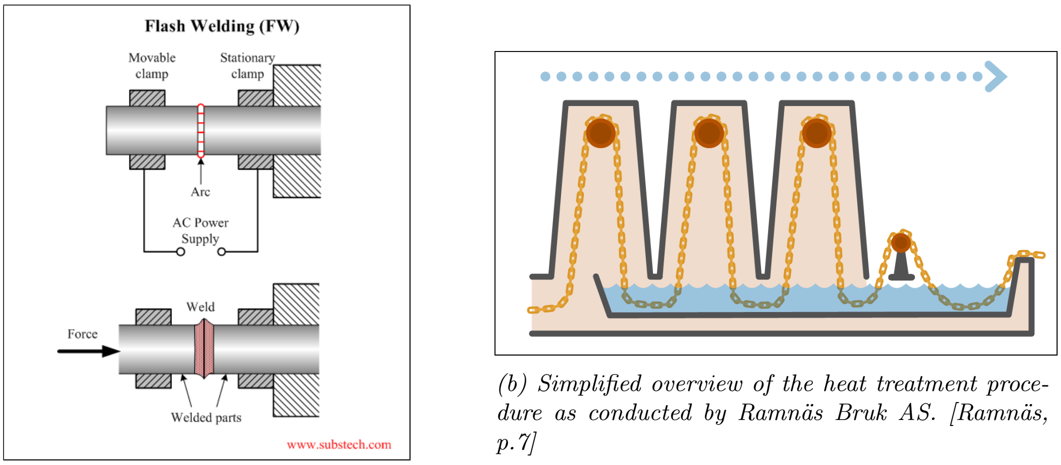

(a) The flash welding process. [SubsTech]

(b) Simplified overview of the heat treatment procedure as conducted by Ramnäs Bruk AS. [Ramnäs, p.7]

Figure 2.5: Production method.

After welding, the chains are subject to heat treatment. This process starts by heating the chain, then quenching it, and reheating it again to temperatures around 570 degrees centigrade. The system currently in use at Ramnäs Bruk AS is portrayed in Figure 2.5b. As can bee seen, the chains are driven through a series of heating towers before being quenched in the water. The result is an increase in toughness and reduction of hardness [Bjørnsen, 2014, p.10]. By changing the exposure times at the different stages, the material properties can be controlled.

After the heat treatment, each length of chain is subjected to proof loading, and must pass this test without fracture. The magnitude of the load depends on the chain diameter, and is specified in [DNV-OS-E302, p.22]. The load may exceed the minimum load by 15%. If a chain link fails, the two links it was connected to shall be subject to a breaking load test. The loading is specified in the same table as the proof loading. The load must be applied for a minimum of 30 seconds, and the test is passed if no signs of fracture are detected. The breaking load tests are not only conducted when a proof loading test is failed, but also at intervals specified in [DNV-OS-E302, p.22]. As an example, a chain that has links with diameter of 112 - 124mm, shall have chain links every 222m sampled. After these tests, the chain is cleaned by shot-blasting the surface, which also introduces compressive residual stresses.

As the chains are subject to many different requirements as specified in ISO1704 and DNV-OS-E302, a series of non-destructive tests are conducted after the proof loading. Before being shaped, the steel bars are inspected by magnetic particle inspection, eddy current testing and ultrasonic testing. This is in order to identify any discontinuities in the material, such as cracks. If the material is found to be free of flaws, the manufacturing process proceeds as described above. When the chains are finished, visual inspection is conducted, and control measurements are made. The measurements are conducted in accordance with DNV-OS-E302, while the chain is loaded with 10% proof loading, and can be summarized as follows:

- A five link length may not be shorter than the given tolerance; minimum 22 times and maximum 22.5 times the diameter of the chain.
- 5% of the chain length of each link shall be measured.
- Diameter measured at the crown cannot have a negative tolerance, and may not exceed 5% of the positive tolerance.
- Largest diameter of flash-butt weld area may not exceed 15% of nominal chain diameter.
- Outside length and width shall not exceed ±2.5%.
- If one or two links fail the tolerance requirements, 20 more links on each side of the affected links shall be measured. If a third link fails, all links shall have the failed dimension measured.

The chains also need to be subject to mechanical testing. The procedures are described in [DNV-OS-E302, p.19]. A test sample is a chain link made as part of the chain cable. From each sample, one tensile and 9 Charpy V-notch test specimens are made. The tensile and three of the Charpy specimens are taken from the straight length on the opposite side of the flash butt weld (section B-B, Figure 2.6. The next three are from the area across the flash-butt weld (section a-a, Figure 2.6, and the last three are from the outer bend of the chain, one third of the radius below the surface(section c-c, Figure 2.6.

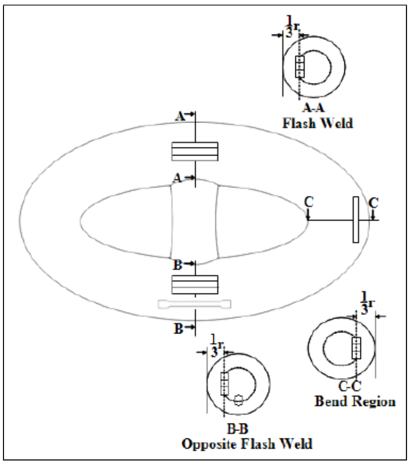

Figure 2.6: Locations where test specimens are taken from. [DNV-OS-E302, p.20]

The chain links are made of steel, and there are currently five different steel grades in use [DNV-OS-E302, p.23]. They are graded according to the The International Association of Classification Society (IACS) [Bjørnsen, 2014, p.11], and are therefore denoted by the letter 'R' with a number. The steel grades R3S, R4, R4S and R5 are considered high strength steels, as their yield strength is above 460 MPa. The material data is recreated in Table 2.2, but excluding the Charpy V-notch data.

Table 2.2: Mechanical properties of steels, as seen in [DNV-OS-E302, p.23]

Grade	**Yield Stress, R_e [MPa]**	**Tensile Strength, R_m [MPa]**	**Elongation, A_5 [%]**	**Reduction of Area, Z [%]**
R3	410	690	17	50
R3S	490	770	15	50
R4	580	860	12	50
R4S	700	960	12	50
R5	760	1000	12	50

The geometry of a studless link is governed by , and the dimensions are seen in Figure 2.7.

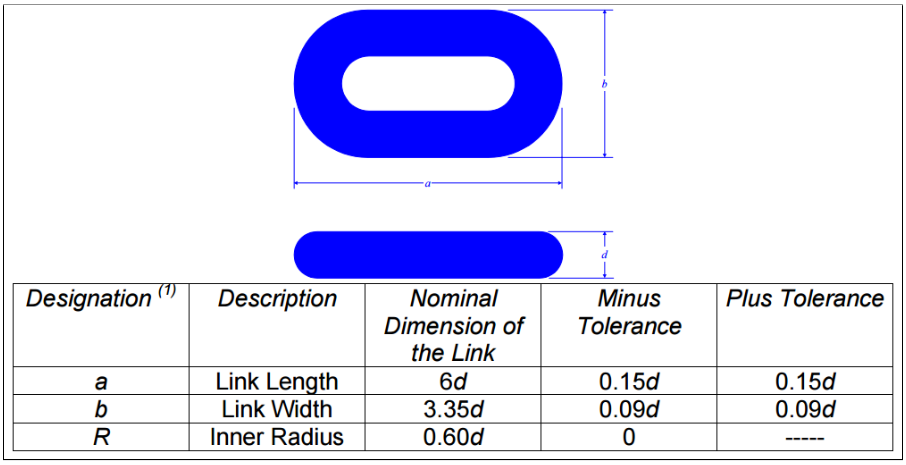

Designation [(1)]	*Description*	*Nominal Dimension of the Link*	*Minus Tolerance*	*Plus Tolerance*
a	Link Length	6*d*	0.15*d*	0.15*d*
b	Link Width	3.35*d*	0.09*d*	0.09*d*
R	Inner Radius	0.60*d*	0	-----

Figure 2.7: Chain geometry specifications. [, p.14]

Wire Rope

Wire ropes in use in mooring lines today, are multi-strand or single-strand [Keshavarz, 2011, p.14]. A strand is a group of wires which are wound in a helical pattern. The axial stiffness and flexibility of the wire rope depends on the pitch angle of the winding. There are two different main types of wire rope; multi-strand and single-strand. Multi-strand wire ropes are most common in temporary moorings, while single-strand wire ropes are primarily used in permanent moorings.

The six-strand wire rope is a common multi-strand wire rope and it is mostly being used in the offshore industry today [Keshavarz, 2011, p.15]. Depending on the pattern the wire ropes are wound in, they can be torque balanced or not. Multi-strand ropes can have a fiber or metallic core. Two common types of metallic cores are independent wire rope cores (IWRC) and wire-strand cores (WRC), of which IWRC is the most used in heavy marine applications.

Spiral strand wire ropes, as compared to six-strand wire ropes are usually torque balanced. This is an attractive feature for permanent moorings, as it prevents the rope from twisting during loading, which makes the line more fatigue resistant.

To improve corrosion resistance, the wires can be sheathed with polyurethane coating, have added zinc filler wires or be galvanized [Keshavarz, 2011, p.15].

Synthetic Fiber Ropes

The use of synthetic fiber ropes has become more common, as the operational sea depth has increased, and the different ropes have been qualified for use. The yield strength and the ultimate tensile stress is usually between 1860-1570 MPa. Synthetic fiber ropes are made of visco-elastic materials, and their stiffness characteristics are therefore not constant. They may vary with load magnitude, number of load cycles and frequency of load cycles [Europe, 2006, p.51]. They may also creep.

2.3 Mooring System Design Analysis

This section will describe the current practice for designing mooring systems, and the analyses necessary in order to do so. The section is based on [DNV-OS-E301]

The mooring systems are designed in accordance with three design criteria formulated from limit states:

ULS Ultimate limit state, which ensures the mooring lines can withstand extreme environmental loads.

ALS Accidental limit state, ensures that the mooring system has the capacity to withstand the failure of one mooring line, thruster or thruster system.

FLS Fatigue limit state, ensures that each individual mooring line can withstand the cyclic loading and resulting fatigue damage.

Each limit state is formulated as a design equation or inequality of the form Eq. 2.1a [DNV-OS-E301, p.36], where Design Capacity, D_C and Design Load-Effect,D_L, are defined in Eq. 2.1b and Eq. 2.1c. In order for a mooring system to be approved for service, it must fulfill the criteria for all three limit states.

$$D_C - D_L \geq 0 \tag{2.1a}$$

$$D_C = (\text{Characteristic Capacity})/(\text{Partial Safety Factor on Capacity}) \tag{2.1b}$$

$$D_L = (\text{Characteristic Load Effect}) \cdot (\text{Partial Safety Factor on Load Effect}) \tag{2.1c}$$

The characteristic values are calculated in different ways depending on which limit state is being studied. The partial safety factors have varying values depending on the type of analyses performed, dynamic or quasi static, as well as the consequence class, with a value varying from 1.1 to 2.0. There are two consequence classes defined in [DNV-OS-E301, p.45], reproduced below.

Class 1 Where mooring system failure is unlikely to lead to unacceptable consequences such as loss of life, collision with an adjacent platform, uncontrolled outflow of oil or gas, capsize or sinking. [DNV-OS-E301, p.45]

Class 2 Where mooring system failure may lead to any of the consequences outlined in Class 1. [DNV-OS-E301, p.45]

The fatigue limit state does not operate with the aforementioned consequence classes, but instead considers the two cases of single and multiple line failure. The fatigue limit state criterion will be further elaborated in the theory section where the state of the art fatigue calculation methods for mooring chains will be discussed, Section 3.4.3.

2.3.1 Analysis types

In order to design the mooring system, it is necessary to know the forces acting on the system with varying loads. When designing the mooring systems, three different analysis methods are usually applied:

- Static
- Quasi-static
- Dynamic

In a static analysis, the seabed is assumed horizontal, and line dynamics ignored [Keshavarz, 2011, p.21].

The quasi static design method is more complex than the static, and generally two different methods are used; either a time-domain analysis or a frequency response analysis. In the time-domain analysis, the equations of motion are integrated over the time domain, and the effect of added mass and dampening are therefore included [Keshavarz, 2011, p.25]. The frequency domain solutions linearize the stiffness and dampening of the system, which makes them unable to include the non linear effects that occur. The frequency domain analysis is mostly used in fatigue analyses with moderate environmental loading [Bjørnsen, 2014, p.35].

For the dynamic analysis, the initial state of the system is first calculated by a static analysis, upon which the external load is later applied.

The DNV GL standard OS-E301 requires a dynamic analysis, but states that a quasi-static analysis may be acceptable if it can be demonstrated that the line dynamics are negligible [DNV-OS-E301, p.39].

2.3.2 Environmental Loads

The moorings systems are attached to offshore structures, who in turn are subject to environmental loads. DNV GL's standard on position mooring systems, take the following environmental conditions and loads into account [DNV-OS-E301, p.19]:

- Waves
- Wind
- Currents
- Marine growth
- Tide and storm surge
- Earthquake
- Temperature differences
- Snow and ice

The wave loads are considered with a return period of 100 years, and includes a set of combinations of significant wave height and peak periods along this 100 year contour [DNV-OS-E301, p.20]. Ship shaped units are sensitive to low frequency motion, and sea states with low peak period could therefore be critical.

The wind loads are also considered with 100 year return periods. The wind load is divided into two components, the mean wind speed, and gusts. Mean winds are treated as a steady component from the load, and are represented as the 1-hour mean wind speed 10m above sea level, while gusts are time varying and described by a wind gust spectrum.

The surface current speeds are considered with 10 year return periods, and are based on marginal distributions of current speeds at the location where the unit will be deployed. The most common categories are tidal currents, circulational currents (associated with oceanic circulational patterns), wind generated currents, loop and eddy currents and solition currents [DNV-OS-E301, p.27].

Some examples of the values given by DNV GL for the environmental loads on the Norwegian continental shelf are seen in Table 2.3 [DNV-OS-E301, p.21-28].

Table 2.3: Examples of environmental loading, with their characteristic values [DNV-OS-E301, p.21-28]

Environmental load		**Return period**	**The Norwegian Sea (Haltenbanken)**	**The North Sea (Troll)**	**The North Sea (Ekofisk)**
Wave	Significant wave height [m]	100 years	16.5	15.0	14.0
	Wave period, T_p [s]	100 years	17.0 - 19.0	15.5-17.5	15.0-17.0
Wind	Wind speed [m/s]	100 years	37.0	40.5	34.0
Current	Surface current speed [m/s]	10 years	0.9	1.5	0.6

2.3.3 Loading Modes in Chains

The dominant mode of loading for chains is tensile loading. Twisting of the chains can also occur, however it is shown that even a large twist on the chain has a limited effect on the fatigue life of a chain [Ridge et al., 2011]. A notable exception is the Dalia FPSO, where it is believed a hockel formed on the chain, which caused the load to be taken across the link, instead of end to end as normal [Ma et al., 2013].

Another mode of loading reached infamy in 2002, when three of the mooring lines holding the Girassol Loading Boy failed at the same time, after a mere 235 days of service [Jean et al., 2005]. This has later been attributed to what has become known as out of plane bending. The phenomenon occurs, when the chain links lock together, resulting in the mooring line as a whole, or a section, starting to act similar to a beam, causing the chain links to bend where they would usually rotate freely relative to each other. The locking is attributed to two different causes. The first is the proof loading of the chains. During the proof loading, the chains are subject to a high load, which permanently deforms the contact surface between the chains. The deformed surface becomes a flatter, elliptically shaped surface, which restricts the relative rotation of the two chains. This deformed surface, combined with a high tensile loading, which will cause a higher frictional force between the chains, lock them in place relative to each other. [Jean et al., 2005, p.3]. The resulting bending from the locking mechanism can be seen in Figure 2.8.

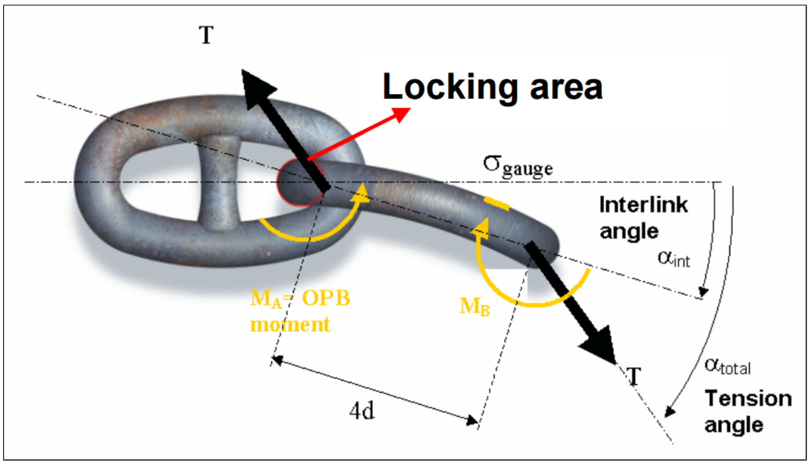

Figure 2.8: Out of Plane bending of Chain Link. [Jean et al., 2005, p.4]

Chapter 3

Theory

3.1 Fatigue in Metallic Materials

Mechanical failures due to fatigue have been subject to research for more than 150 years. Motivated by railway axle failures, August Wöhler [Schütz, 1996] began developing design strategies for avoiding fatigue failures. He proved that the cyclical life of a component not only varied with the cyclic streses, but also the mean stresses. His extensive experimental work and tables of data, is considered the background for the Stress-Life curves, often called Wöhler curves, which will be introduced in a later section. [Dowling, p.399]

There are three major approaches to analyse and design against fatigue failures; stress, strain and fracture mechanics approach. The stress-based approach, focuses on nominal stresses, and considers the effects of mean stress, and stress increasing effects, such as notches and grooves. The strain-based approach involves a more detailed analysis of the localized yielding around stress raisers which may occur during cyclic loading. The fracture mechanics approach, treats the fatigue failure as a consequence of growing cracks, and analyses them by the use of fracture mechanics. [Dowling, p.399]. The strain based approach is primarily used in cases where there are high stresses and a large amount of plasticity. This is not the case for the problem studied in this thesis, and will therefore not be discussed further.

The fatigue lives is conventionally divided into two different periods; crack initiation- (N_i) and crack propagation period (N_p). Crack initiation is conventionally described to occur due to the movement of slip planes. They will move relative to each other, resulting in multiple inclusions and extrusions, which in turn can result in a crack. Cracks can also initiate at internal impurities in the material.

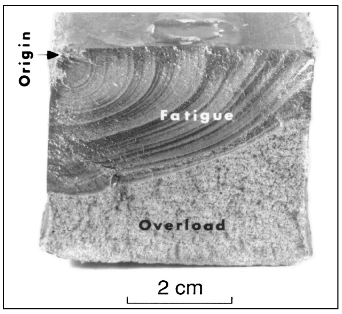

(a) Photography of beachmarks. [ASME International, a]

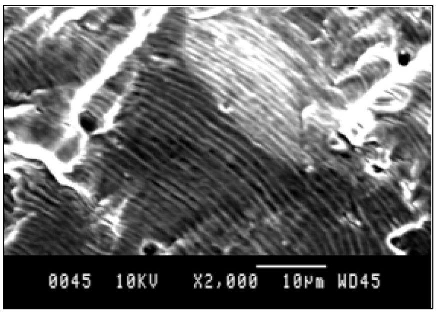

(b) Microscopic photography of striations. [Gunnar Härkegård, 2015]

While the crack is propagating, it will create beach marks and, or striations, depending on the mode of loading. Beach marks occur, when the texture of the fracture surface changes as a result of the crack being delayed or accelerated [Dowling, p.422]. This can occur due to alternating stress levels, temperature or chemical environment. If beach marks occur they are usually large, as seen in Figure 3.1a, and can be seen without using microscopes. Striations, Figure 3.1b usually occur in ductile materials [Dowling, p.423], and show the progress of a crack with each cycle. The most accepted explanation for the existence of striations, is that they are created by the successive crack tip blunting and sharpening occurring for each load cycle [ASME International, b, p.1].

3.2 Fatigue Life Curves

An important concept when considering fatigue, is the fatigue life curves. Wöhler had produced a wealth of experimental data considering the life of a component, with respect to the applied stress. By using this data, Basquin formulated Basquin's law, Eq. 3.1, which shows a logarithmic relation between the stress amplitude applied to the component and it's life.

$$\sigma_a = A \cdot N_f^B \tag{3.1}$$

Where N_f is the final life of the component,σ_a is the nominal stress amplitude and A and B are fitting constants. The use of Stress-Life curves (SN-curves), is today an important part of the fatigue life estimation, by using the curve data given in different standards such as DNV GL RP-001 from DNV GL and BS7608 from the British Standard Institution, or generating a curve by conducting fatigue experiments.

The most common form of Eq. 3.1 is:

$$\sigma_a = \sigma'_f (2N_f)^b \tag{3.2}$$

Where σ'_f is the fatigue strength coefficient and b is the fatigue strength exponent [Ås, 2006, p.7]. These values are usually tabulated as material properties [Dowling, p.405]. Basquin's law is only valid in the high cycle fatigue region, which will be explained next.

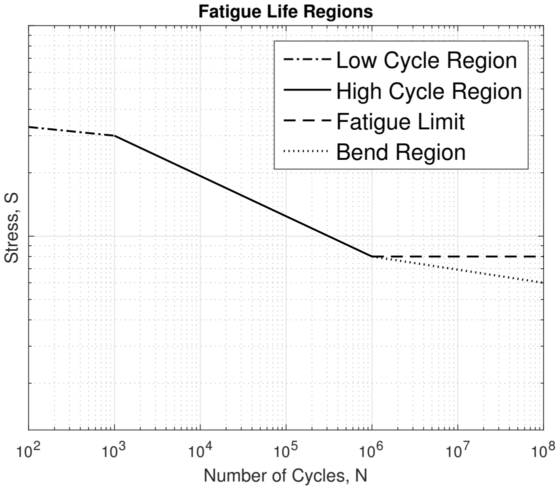

Figure 3.2: Fatigue Life Regions.

The fatigue effects on a component is usually divided into low cycle and high cycle fatigue, as seen in Figure 3.2. Low cycle fatigue occurs when the component is subject to large stresses, and life is less than 10^3 cycles. High cycle fatigue is in the region between 10^3 to 10^6 cycles. When the life extends beyond 10^6, for a given stress level, the stress is said to be below the fatigue limit, and any cycles in this region does not reduce the life of the component. When the component is subject to environmental effects, such as corrosion, however, a fatigue limit does not necessarily exist. In these cases the stress-life curve will instead show a bend beyond where the material would usually exhibit a fatigue limit.

3.2.1 Effect of Corrosion

There are many different types of corrosion. The most common is electrochemical corrosion, which causes the loss of material and generates corrosion pits on the surface of the affected component. Other types of corrosion are microbiologically influenced corrosion (Microbiologically Influenced Corrosion (MIC)), stress corrosion cracking (Stress Corrosion Cracking (SCC)), sulphide stress corrosion cracking (Sulphide Stress Corrosion Cracking (SSCC)) and hydrogen embrittlement. The effect of corrosion is extensively covered by Kristin Hanem Tømmervåg, and the reader is referred to her Master Thesis for further study on this subject. Crack initiation from corrosion pits, however, will be described further.

Crack Initiation from Corrosion Pits

The effect of corrosion pits on crack initiation and fatigue life have been extensively researched. The earliest attempts at describing the pit to crack transition were made by Kondo [1989]. He suggests that a pit will become a crack when the pit reaches a certain depth, and the crack growth rate exceeds the pit growth rate. This concept was further developed by Wei [2000], where the first criterion was changed so that the cyclic stress intensity range, ΔK, has to exceed the fatigue crack growth threshold. The criteria can be written as Eq. 3.3

$$\Delta K \geq \Delta K_{th}, \left(\frac{da}{dt}\right)_{crack} \geq \left(\frac{da}{dt}\right)_{pit} \tag{3.3}$$

Zhang et al. [2013] performed a literature study on the subject. It was concluded that the the amount of corrosion pits that form vary with the stress amplitude; a higher stress amplitude causes more corrosion pits to form. Also, it was found that cracks initiating from corrosion pits do not necessarily originate from the bottom of the pit, but rather from the point that has the biggest Stress Concentration Factor (SCF).

3.2.2 Load Effects

The fatigue life of a component varies with the loading it is subjected to. It is not wholly dependent on the stress amplitude however, but also varies with the mean stress applied. Different models to account for this effect has been proposed, such as the one by Morrow [Dowling, p.455]:

$$\frac{\sigma_a}{\sigma_{ar}} + \frac{\sigma_m}{\sigma'_f} = 1 \tag{3.4}$$

Where σ_{ar} is the equivalent zero mean stress amplitude, and σ_m is the applied mean stress. Another model was suggested by Walker, given for $\sigma_{max>0}$:

$$\sigma_{ar} = \sigma_{max}^{1-\gamma}\sigma_a^{\gamma} \tag{3.5}$$

Where γ is a fitting parameter which varies with the material of the component.

If the component is subject to a non constant amplitude loading, it is necessary to approximate the fatigue life by using a cummulative rule such as the Palmgren-Miner rule. This method sums the fraction of the number of cycles at a given stress level over it's total life for the given stress, as seen in Eq. 3.6.

$$\frac{N_1}{N_{f_1}} + ... + \frac{N_n}{N_{f_n}} = \sum_{i=1}^{i=n} \frac{N_i}{N_{f_i}} = D \leq \eta \tag{3.6}$$

Where D is defined as the accumulated damage, and η is the usage factor or the design fatigue factor of the component, as seen in [DNV-RP-C203, p.14]. In Palmgren's original formulation, η was set equal to 1.

3.2.3 Residual Stresses and Stress Raisers

Residual stresses can be defined as the stresses generated in a body during manufacturing, material processing or service that persist even in the absence of an external loading. The main mechanisms for the generation of residual stresses can be classified into three different origins [Sharpe, 2008]:

- Differential plastic flow
- Differential cooling rates
- Metallurgic effects due to phase transformation and volume changes

The second and third effect are results from micro structural changes in the material, and originate from production of the component. It can also occur if the component is subject to large temperature changes during service. The first effect either occurs during manufacturing, by working the material, or when the component is overloaded either in service life of during testing. An example of residual stresses occurring during testing is during proof loading of an offshore chain.

Having tensile residual stresses in a component will result in the reduction of it's fatigue life, while compressive stresses may prove beneficial to the component life. The detrimental effect of the tensile stress can be accounted for by treating it as an increase in the mean stress applied to the component [Totten, 2002, p.43].

Residual stresses can be relaxed in a multitude of ways. Elastic residual stresses can be converted to micro plastic strain through dislocation slip, grain boundary sliding, creep or diffusion creep. It can also be released by the formation and propagation of cracks [Totten, 2002].

As the residual stresses are detrimental to the fatigue life of the component, quantifying the magnitude of these stresses is therefore important. This can be conducted by performing a finite element analysis, or measuring them in the component. Residual stresses can be measured by performing x-ray diffraction tests, or cutting the component and measuring the amount of relaxation.

3.3 Fracture Mechanics

The effect of materials failing before their theoretical cohesive strength is spent, has been shown throughout history by many scientists, such as Leonardo da Vinci, Griffith and others. It was proposed that this discrepancy was due to flaws in the material, and the first quantitative evidence was given by Inglis [Inglis, 1997] who analyzed elliptical holes in flat plates. He found that the maximum stress concentration could be described by a constant k, stress concentration factor, and the far field stress, as seen below:

$$\sigma_a = S\left(1 + 2\sqrt{\frac{a}{\rho}}\right) \tag{3.7}$$

As the radius of curvature of the crack tip, ρ, approaches zero, the stress approaches infinity. A sharp crack in a material should therefore fail under even an infinitesimal load. This contradiction motivated Griffith to form the Griffith energy balance, which considers the energy required to form a crack as a relation between the potential energy from internal strain and external forces, and the energy required to create new surfaces.

3.3.1 Stress Analysis of Cracks

It is possible to derive closed-form analytical solutions for the stresses around a crack for certain specific configurations, assuming linear elastic material behavior. Westergaard [Anderson, 2007, p.96] published one such solution, where it is shown that the stress in polar coordinates can be given as:

$$\sigma_{ij} = \left(\frac{k}{\sqrt{r}}\right) f_{ij}(\theta) + \sum_{m=0}^{\inf} A_m r^{\frac{m}{2}} g_{ij}^{(m)}(\theta) \tag{3.8}$$

Where:
σ_{ij} = Stress tensor
f_{ij} = Dimensionless function of θ
k = Constant
It is seen that the leading term approaches infinity while the other terms stay finite or approach zero. Stress at the crack tip therefore varies with the singularity $\frac{1}{\sqrt{r}}$.

The Stress Intensity Factor (Stress Intensity Factor (SIF))

There are three types of loading a crack can experience, Mode I, Mode II and Mode III. As seen in Figure 3.3 [Anderson, 2007, p. 43]. The stress concentration factor k, and the function f, change depending on the loading that is present.

Resulting in the following general stress equation when r goes to zero:

$$\lim_{r\to 0} \sigma_{ij}^{mode} = \frac{K_{mode}}{\sqrt{2\pi r}} f_{ij}^{mode}(\theta) \tag{3.9}$$

As the stress was found assuming linear elastic theory, the individual contributions from the different modes of loading may be summed by the principle of superposition:

$$\sigma_{ij}^{mode} = \sigma_{ij}^{(I)} + \sigma_{ij}^{(II)} + \sigma_{ij}^{(III)} \tag{3.10}$$

Also, as the principle of superposition is valid, the stress intensity factors resulting from two different loads on the same geometry may be summed:

$$K_I^{total} = K_I^1 + K_I^2 \tag{3.11}$$

Handbook solutions for stress intensity factors have been developed over the years. The different authors have chosen a variety of ways to express SIF and the geometry function, F. As an

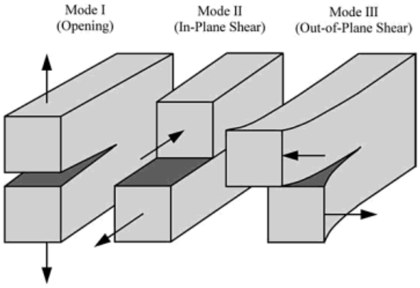

Figure 3.3: Loading modes for cracks, [Anderson, 2007, p.43]

example, Eq. 3.12a shows the form employed by Raju and Newman [1979], while Eq. 3.12a shows Shin and Cai's [2004] definition.

$$K_I = SF_I\left(\frac{a}{t}, \frac{a}{c}, \phi\right)\sqrt{\left(\pi\frac{a}{Q}\right)} \tag{3.12a}$$

$$K_I = SF_I\sqrt{\pi a} \tag{3.12b}$$

The form seen in Eq. 3.12b, will be applied for all results in this thesis, and any other handbook solution used will be converted to this form.

3.3.2 The J Contour Integral

The J contour integral was presented by Rice [Rice, 1968], and is path-independent for any path Γ. The integral equation, Eq. 3.13, can by Green's theorem be transformed into a surface integral for the three dimensional case.

$$J = \int_\Gamma \left(w dy - T_i\frac{u_i}{x}ds\right) \tag{3.13}$$

Where [Anderson, 2007, p.110]:

w	Strain energy density
T_i	components of the traction vector
u_i	components of displacement vector
ds	length increment along the path Γ

In linear fracture mechanics, the J-integral is equivalent to the energy release rate, and it can therefore be used to calculate the stress intensity factor through Eq. 3.14 for the case of plane strain.

$$K_I = \sqrt{\frac{J \cdot E}{(1-v^2)}} \tag{3.14}$$

When a crack intersects a free surface, a corner forms, which also shows a singularity. It does not have the same power as the regular $r^{\frac{1}{2}}$ singularity. In an elastic material, the singularity must vary with $\frac{1}{2}$ in order to be non-zero [Anderson, 2007, p.584].

3.3.3 Fracture Mechanical Fatigue Approach and Crack Propagation

For the past decades, many papers have been published on the matter of crack propagation and the different aspects of this phenomenon. Many different models have been proposed, and they can be represented on the general form [Anderson, 2007, p. 452]:

$$\frac{da}{dN} = f_1(\Delta K, R) \tag{3.15}$$

The number of cycles required to propagate the crack can therefore be expressed as [Anderson, 2007, p. 452]:

$$\int_{a_0}^{a_f} \frac{1}{f_1(\Delta K, R)} da \tag{3.16}$$

Where [Anderson, 2007, p. 452]:

$\Delta K \ = (K_{max} - K_{min}) = \Delta S\ F(a)\ \sqrt(\pi a)$

$R \quad = K_{min}/K_{max}$

Empirical Crack Growth Relationships

Figure (3.4), shows a log-log plot of da/dN against ΔK describing typical fatigue crack behaviour. The graph can be divided into three regions, where the middle region shows an almost linear behaviour. It can be observed that the first region approaches zero as ΔK approaches it's minimum value, known as the threshold. This indicates that as long as $\Delta K < \Delta K_{th}$ the crack will not propagate. For many materials, the growth rate increases rapidly in the third region. There are many hypothesis' regarding this behavior, of which the source either being microscopic effects or that it is infact not real but a result of the crack-tip plasticity influencing the true driving force for fatigue as ΔK becomes high. At high K values, ΔJ might be better to characterize fatigue.

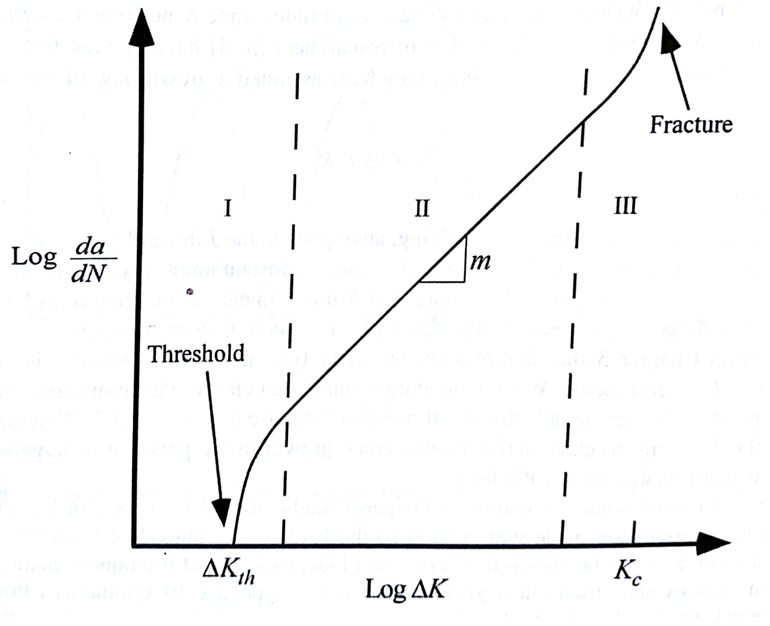

Figure 3.4: Stages of crack growth

The linear, or second, region of the graph can be described by a power law, and was first proposed by Paris and Erdogan [Paris and Erdogan, 1963]:

$$\frac{da}{dN} = C(\Delta K)^m \tag{3.17}$$

They applied an m of four, but it as been shown that it can range from two to four in most metals in non-corrosive environments. In order to account for the regions I and III, Forman [Klesnil and Lukáš, 1972] proposed the following equation:

$$\frac{da}{dN} = \frac{C(\Delta K)^m}{(1-R)K_c - \Delta K} \tag{3.18}$$

The equation assumes however that the increased growth in region III is due to the superposition between fatigue and fracture, not plastic zone effects.

By integrating the empirical crack growth laws, one can find the life of a component. For Paris' Law, the equation becomes:

$$\Delta N = \int_{a_i}^{a_f} \frac{1}{C(\Delta S \cdot F(a)\sqrt{\pi a})^m} da \tag{3.19}$$

Eq. 3.19 can be solved by numerical integration, or it can be simplified by assuming that the geometry function, F, does not vary with the crack depth. In that case, the following equation, yields the life of the component[Sirevaag, 2015, p. 23]:

$$n(a_i, a_f) = \frac{a_i}{da/dn_i}\left(\frac{1-(a_i/a_f)^{\frac{m}{2}-1}}{\frac{m}{2}-1}\right) \tag{3.20}$$

Crack Front Shape

The shape of the crack front has a large impact on the SIF, and how the shape of the crack front changes as a crack propagates is therefore important to correctly estimate the fatigue life of a component. The effect on surface cracks in rods were investigated by Lin and Smith [1997], Couroneau and Royer [1998], later by Shin and Cai [2004] and most recently by Toribio et al. [2009]. Both Shin and Toribio only performed analyses with tensile loading, while Couroneau and Lin also included bending load. The results from the analyses performed by the aforementioned authors is seen in Figure 3.5b. It was found that the crack front shape varies with both the loading applied and the crack growth parameters, resulting in different crack growth shapes for bending, tension and crack growth parameter m. Toribio et al. [2009] shows that the crack front shape further depends on whether the rods have their ends constrained or free, the aforementioned being almost twice as large as the last towards the end of the crack growth.

Couroneau's solution is further elaborated in Appendix B.

Mean Stress

Fatigue Crack Growth increases with increasing stress ratio, R. Walker suggested taking this into account the same way as discussed earlier, but using K instead of the stress. Verified in [Dowling].

$$\Delta\bar{K} = K_{max}(1-R)^\gamma \tag{3.21}$$

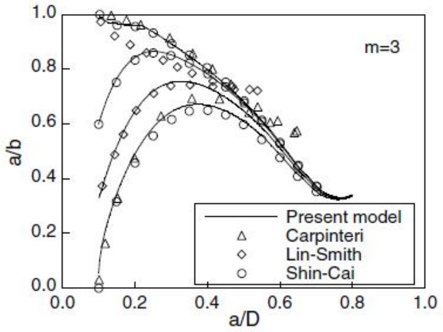

(a) Comparison between the different solutions currently present in literature. Loading is tensile, ends are free, and m=3. [Toribio et al., 2009, p.629]

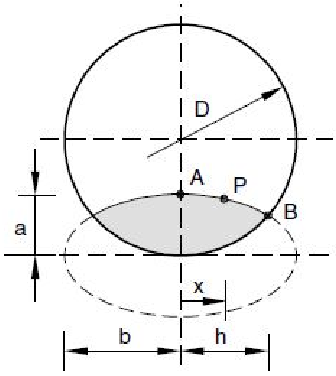

(b) Description of nomenclature. [Toribio et al., 2009, p.629]

Crack Closure

In the 1970's it was observed by Elber [Anderson, 2007, p. 455] that when a crack is subject to a cyclical loading, the compliance experienced during the last part of the compression was actually closer to that of an uncracked specimen than a cracked specimen. Elber believed this to be caused by the crack surfaces coming in contact during compression at loads greater than zero but still low, and it led to extensive research into the phenomenon now known as crack closure.

Elber hypothesized that there existed a portion of the cycle known as K_{op}, where once the K was below this limit, it does not contribute to the crack growth. The following variables were defined [Anderson, 2007, p. 457]:

$$\Delta K_{eff} \equiv K_{max} - K_{op}$$

3.4 Current Fatigue Calculation Methods

The fatigue life calculation methods in use in the industry today can be summarized in two approaches; the stress-life curve, and the fracture mechanics approach. In order to describe the current norm of fatigue calculations, the standards from DNV GL and British Standard Institution British Standard Institution (BSI) will be used. The theory used in the respective approaches, is described in Section 3, and this section is therefore focusing on the methodology.

3.4.1 Stress-Life Approach

The Stress Life (SN) approach, naturally revolves around the use of SN-curves in order to determine the fatigue life of the component. The SN-curves are generated by testing small specimens until failure, and using the stress and life data obtained to generate an SN-curve, as described in Section 3.2. Over the years, SN data has been meticulously gathered, and design curves have been made for different components and geometries. These are published in the standards by both DNV GL and BSI. DNV GL operate with three different concepts of SN-curves [DNV-RP-C203, p.14]:

- Nominal stress-life curves
- Hot spot stress-life curves
- Notch stress-life curves

The nominal stress is understood as stresses found in classical theory [DNV-RP-C203, p.14]. When applying the nominal stress method, the increased local stress due to the presence of, for example, a weld is not included. However, if the structure globally causes an increase in the stress locally, this should be accounted for by multiplying the nominal stress with the relevant stress concentration factor (SCF), as seen below.

$$\sigma_{local} = SCF \cdot \sigma_{nominal}$$

There are changes in how to define the local stress, depending on what kind of component is being analyzed, and the reader is referred to the [DNV-RP-C203, p.15] for more details.

The hot spot stresses, are the geometric stresses resulting from stress raisers existing in the component, such as notches. The local stress is usually measured at two different points, a specified distance away from the modelled detail, and the stresses extrapolated in towards the detail. There are however, multiple definitions of the hot spot stress, depending on the detail in question. The stresses themselves are usually found with the finite element method, and are calculated assuming a linear material behaviour.

The notch stress-life curves are used together with a method called the effective notch stress method. Here, the notches, or local weld geometries are replaced by "effective notches" of varying radius. The notch stress is the total stress obtained in these regions. This method is primarily used for welded details, and will therefore not be elaborated further.

3.4.2 Fracture Mechanics Approach

The standard BS7910 is a guide to help assess flaws in metallic structures. It is therefore written with the intention of addressing structures that have existing flaws, and presents a method for fatigue assessment with this in mind. The method is based on a fracture mechanic analysis of the component and any existing flaws. The procedure is summarized below:

1. Decide and describe the crack growth model to be used. Including the threshold value for the stress intensity factor, ΔK_{th}.
2. Determine the stress range the component is subjected to.
3. Determine ΔK for the given stress range and flaw of the component. This can be done from published solutions, numerical analysis or weight function techniques.
4. Estimate the growth of the crack for one cycle by using the value of ΔK. The crack dimension should then be increased by Δa.
5. Determine the stress intensity factor for the new crack geometry.
6. Check if new crack size exceeds allowed crack dimensions. If the new dimensions are accepted, reiterate the procedure from (4). If the fatigue design life is reached, and the crack size limit to growth is not exceeded, the flaw is regarded as acceptable.

An alternative method presented in BS7910, is based on a concept introduced as quality categories. These categories define the fatigue strength of flaws in terms of SN curves. The relation is given as:

$$\Delta\sigma^3 N = constant \tag{3.22a}$$

The quality curves are generated for the stress yielding a service life of $2 \cdot 10^6$ cycles. An exerpt with example values for steels has been included in Table 3.1.

When designing the curves, steel and some aluminium materials were used. The validity for different material types could therefore be varying, but it was observed that in dry air environments that the fatigue crack growth in a wide range of ferritic steels is similar, and the standard

Table 3.1: Excerpt of the details of quality category S-N curves table. [BS7910:2013, p.73]

Quality category	**Constant from Eq. 3.22a**	**Equivalent BS 7608 design class**	**Stress range, S for $2 \cdot 10^6$ cycles, [MPa]**
Q1	$1.52 \cdot 10^{12}$	D	91
Q2	$1.04 \cdot 10^{12}$	E	80
Q3	$6.33 \cdot 10^{11}$	F	68
Q4	$4.31 \cdot 10^{11}$	G	60

therefore suggests that the results remain valid. [BS7910:2013, p.88]. The use of the quality category curves, require the conversion of actual flaw dimensions to an effective initial and final flaw parameter, $\bar{a_i}$. The effective crack is defined as an equivalent straight-fronted crack, to the crack in question.

The standard assumes Paris's law to be valid, and uses an m equal to 3, and C = $5.21 \cdot 10^{-13}$ for Eq. 3.19. The m value cannot be changed, but a different C can be accounted for by transforming the stress by Eq. 3.22b. It should be noted that the BS7910 syntax uses A as the crack growth parameter C.

$$S_1 = S\left(\frac{5.21 \cdot 10^{-13}}{C_1}\right)^{1/3} \tag{3.22b}$$

The full procedure can be summarized as follows:

1. Establish the crack growth parameter C.
2. Define the initial and final crack dimensions.
3. Use Figure 3.6a to convert the crack dimensions to effective crack depths.
4. Use Figure 3.6b together with the section thickness B to find S_i when using $\bar{a_i}$, and S_m when using $\bar{a}_{max}$. (Interpolate values if necessary).
5. The total stress is calculated by using Eq. 3.22c. If the $\bar{a}_{max} >> \bar{a_i}$, the contribution from S_m can be neglected, and thus simplifies S to S_i.
6. The quality category is defined as the next below the value of S found in Table 3.1.

$$S = (S_i^3 - S_m^3)^{1/3} \tag{3.22c}$$

3.4.3 Mooring Chain Fatigue Calculations

The current industry practice applied by DNV GL is centered around the SN approach, in order to describe the fatigue limit state as described in Section 2.3. The loading is divided into reference environmental states, and analyses are performed for 10-50 states in order to find the response in the mooring lines [DNV-OS-E301, p.52]:. A discrete probability value is set for each sea state, and the accumulated damage is defined as [DNV-OS-E301, p.50]:

$$d_i = n_i \int_0^\infty \frac{f_{S_i}(s)}{n_c(s)} ds \tag{3.22d}$$

Where:

d_i Accumulated damage.

n_i Number of cycles applied.

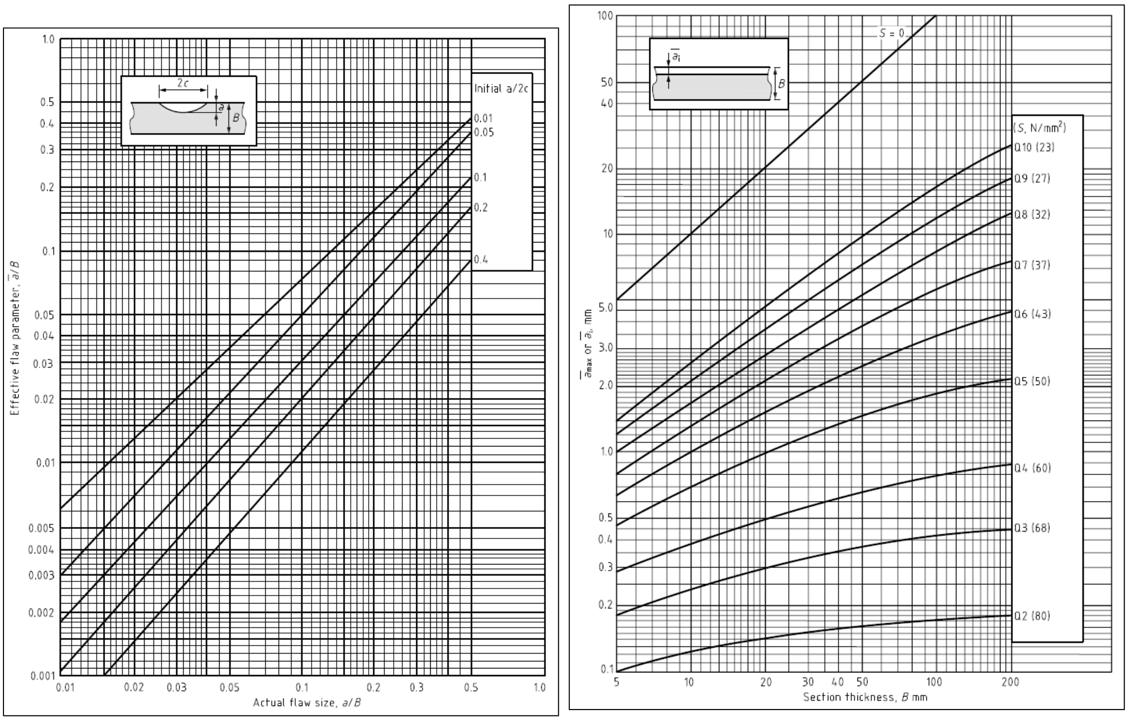

(a) Relation between actual flaw dimensions, and the effective flaw parameter.[BS7910:2013, p.79]

(b) Relation between effective flaw parameter, section thickness and quality category. [BS7910:2013, p.80]

Figure 3.6: BS7910 Quality Category Design Curves. [BS7910:2013, p.79,80]

n_c	Critical number of cycles for component.
f_{S_i}	Probability density of the nominal magnitudes (peak to through) for applied stress cycles.

DNV GL implements fatigue life curves, by using the following formulation:

$$n_c(s) = a_D s^{-m}$$

or in it's linearised form:

$$log(n_c(s)) = log(a_D) - m \cdot log(s)$$

Where,

$n_c(s)$	the critical amount of stress ranges (cycles).
s	the stress range.
a_D	the intercept parameter of the SN-curve.
m	the slope of the S-N curve.

The parameters a_D and m have been found by testing by DNV GL, and their results as seen in the standard are replicated in Table 3.2.

The exception lies with the long term mooring shackles, which should be designed with the B1 SN-curve as seen in DNVGL-RP-C203. According to [Fernández et al., 2014, p.1], these tests were conducted on steels of quality ORQ,R3 and R4, and small chains, with 76mm diameter being the largest tested speciment.

Table 3.2: Fatigue properties of mooring line components, [DNV-OS-E301, p.51], and the DNV B1 design line [DNV-RP-C203, p.21].

Component	a_D	$\boldsymbol{m}$
Stud. chain	$1.2 \cdot 10^{11}$	3.0
Studless chain	$6.0 \cdot 10^{10}$	3.0
Stranded rope	$3.4 \cdot 10^{14}$	3.0
Spiral rope	$1.7 \cdot 10^{17}$	4.8
DNV B1	$1.31 \cdot 10^{15}$	4.0

When Eq. 3.4.3 is applicable for the fatigue properties of the mooring line, the fatigue damage per sea state is described as:

$$d_i = \frac{n_i}{a_D} E[S_i^m] \tag{3.22e}$$

Where $E[S_i^m]$ is the expected value of the nominal stress range, S, raised to the power of m in a reference sea state i. The nominal stress range in the chain is calculated by dividing the tension cycles with the nominal cross section area of a chain, $2\pi d^2/4$. The exact method to calculate the loading is quite complex, and the reader is therefore referred to the DNV GL OS-E-301 standard for details.

The fatigue limit state design equation is given as:

$$1 - d_c \cdot \gamma_F \geq 0 \tag{3.22f}$$

Where,

d_c	Characteristic accumulated fatigue damage.
γ_F	Single safety factor of the fatigue limit state.

The form of the characteristic accumulated fatigue damage varies with the assumptions made with respect to loading on the system, [DNV-OS-E301, p.53], but it can be considered a form of Miner-Palmgren sum.

The aforementioned methodology so far, only describes the case of tension-tension loading, and does not include the effect of other modes of loading such as out of plane bending. For chain links that are frequently located in a chain wheel, it is suggested to apply a SCF of 1.15 to the loading. For any other case, there is no specific procedure outlined, and it is merely stated that the OPB effect can be established by theoretical calculations or testing [DNV-OS-E301, p.52].

Lassen et al. recommend calculating the fatigue contribution from Out of Plane Bending (OPB), or combined OPB and tension, in one of two ways. The first is to apply the hot spot method using the maximum principal stresses in conjunction with finite element analyses and the DNV GL B1 SN-curve. The second is to perform a fracture mechanics analysis as outlined in Section 3.4.2 [Lassen et al., 2009] in conjunction with handbook solutions for cracks in rods. This method is evaluated in Appendix A, together with another proposed simplified fatigue calculation method.

3.5 Fatigue Testing and Results

Ramnäs Bruk AB were the first to attempt to characterize the fatigue behaviour of mooring chains in the early seventies, with 2" chains that they tested in air. In the eighties DNV did their first testing, and in the beginning of the nineties API released a draft of a recommended practice for design, analysis and maintenance of mooring for floating production systems. In their RP, a T-N fatigue curve was given for chains. The standard chain dimensions that are in use today, 6d height with 3.35d width, were introduced by Vicinay in 1993. From the early nineties and throughout the decade, multiple JIP's were conducted, among them one by BOMEL [3,4] and another by NDAI [10,11]. In 2001, Noble Denton created a recommended curve from the result of a JIP conducted between 1997-2001, which featured a fatigue program of chains with diameter 76mm and grade R3 and R4 steel. DNV published their offshore standard for Position Mooring in 2001, with S-N fatigue curves for both studless and studded chains after the completion of the Deepmoor JIP [Fernández et al., 2014, p.2].

3.5.1 Fatigue Performance of R4 and R5 Steels

As a response to the lack of testing conducted on large diameter chains of higher quality steels, Fernández, Storesund and Navas performed such a test, and published their results in 2014 [Fernández et al., 2014]. In total they conducted 19 test, 7 with R4 steel and 12 with R5 steels. The chain diameters varied from 70mm to 171mm. How these tests were performed and their results will be presented in the following sections.

Test Procedure

The test rig consists of a self supporting structure with one reaction end and a force-controlled hydraulic actuator at the other. The links are placed in a tube shaped rubber water tank, which is sealed in the middle of two links. The end links are therefore not in water, and the next links from both sides of the chain are half in air and half in water. Only the center links are covered in water. The rig had a useful span of around 4m. As the chain links are of different lengths, the different diameter chains resulted in a different number of chain links in water. The water in the tank was artificial sea water, made from a sodium chloride concentrate. The tank was oxygenated by an air flow induced by hoses throughout the whole test. The tests were continued until first link failure. [Fernández et al., 2014, p.3]

Test Program

The test program is considered a low cycle, high stress program, and the maximum amount of cycles reached was 3 million. The tests were conducted from 2000 to 2012, and one test performed in 1995. The tests lasted from few days, up to five months.

The load ranges were normalized to the minimum breaking load of the ORQ grade chain. The load varied from 10 to 33% of this reference value. The last two chains tested were pre-soaked for two weeks before testing, in order to create a layer of rust before cycling. The cycling continued until one chain link failed. Figure 3.7 shows two fractured specimens. [Fernández et al., 2014, p.3]

Table 3.3 summarizes the testing details, and which locations they failed at.

Results

As seen in Table 3.3, 9 failures occurred in the bend, 6 in the crown, 3 in the straight section and one test finished without failure. All of the failures except one occurred in a link submerged in water. The paper does, however, not specify which test specimen failed in air. No measurements of crack growth, or inspections of the specimens during testing were conducted, and it is therefore not known how many cycles can be attributed to crack nucleation and crack growth respectively. Two lines were made for the SN diagrams, one with a slope of 3 enforced, and another without enforcing the slope, which resulted in a slope of 2.65.

Table 3.3: Results from the Tension-Tension fatigue program [Fernández et al., 2014, p.3].

Test	**Dia [mm]**	**Design**	**Grade**	**Freq [Hz]**	**Failure Location**	**Links in water**
1	102	Studless	R4	0.6	Bend	2
2	120	Studless	R4	0.4	Bend, Crown	2
3	120	Studless	R4	0.4	Bend	2
4	142	Studless	R4	0.5-0.7	Crown	2
5	171	Studless	R4	0.5	Crown	2
6	120	Studless	R4	0.3	Bend	4
7	152	Studless	R4	0.2	Crown	4
8	149	Studless	R5	0.5	Straight	2
9	127	Studless	R5	0.2	Bend	5
10	157	Studless	R5	0.2	Bend	3
11	70	Studless	R5	0.7	Crown, Bend	9
12	70	Studless	R5	0.7	Straight	9
13	70	Studless	R5	0.5	Crown, Bend	9
14	70	Studless	R5	0.5	Crown	9
15	125	Studless	R5	0.2	Bend	4
16	120	Studless	R5	0.2	Bend	4
17	137	Studless	R5	0.3	Straight	4
18	165	Studless	R5	0.3	Bend	4
19	165	Studless	R5	0.3	No Failure	9
1	70	Stud	R5	0.7	Bend	9

Figure 3.7: Examples of fractured chain specimens. The specimen on the left fractured at the bend, while the specimen on the right fractured at the crown.[Fernández et al., 2014, p.4].

3.6 Crack Growth Data

The crack growth data most commonly used in the offshore industry today, stem from the British Standard 7910, [BS7910:2013]. A study was conducted in cooperation between Vicinay and Agder University College [Lassen et al., 2005], in order to investigate the crack growth behaviour of R4S steel specifically. These results were then compared to the results from BS7910. The procedure and results from [Lassen et al., 2005] will be presented in the following section.

The tests were conducted in three different environments; dry air, sea water with free corrosion and sea water with cathodic protection. The tests were were conducted on eight Compact Tension (CT) specimens, with 25mm thickness and constant amplitude loading applied with a frequency of 0.2Hz and an R ratio of 0.2. The thickness of 25mm was chosen in order to ensure plane strain condition at the crack front [Lassen et al., 2005, p.2]. A sharp crack front was created by spark erosion. The crack growth was measured by an Alternating Current Potential

Table 3.4: List of specimens and test environment.

Specimen	Environment	Cathodic Potential [mV]
0	Dry air	0
1	Free corrosion	0
2	Free Corrosion	0
3	Free Corrosion	0
4	Cathodic Protection	-890
5	Cathodic Protection	-890
6	Cathodic Protection	-1100
7	Free Corrosion	0

Drop (ACPD) system, and a linear relation between the potential drop and the crack growth was assumed. The method is not accurate in the early crack growth stage, but has a high accuracy in the region of growth where beachmarks are made. Some of the readings were also corroborated by a replica method and microscopy [Lassen et al., 2005, p.2].

Table 3.4 shows a list of the specimens, and which environments they were tested in.

The experiments carried out for free corrosion in sea water showed a good correlation between the mean crack growth rates, but the slope of the regressed curve was not as steep as the one given in BS7910. This will have large consequences if the results are later extrapolated, as can be seen in Figure 3.8b.

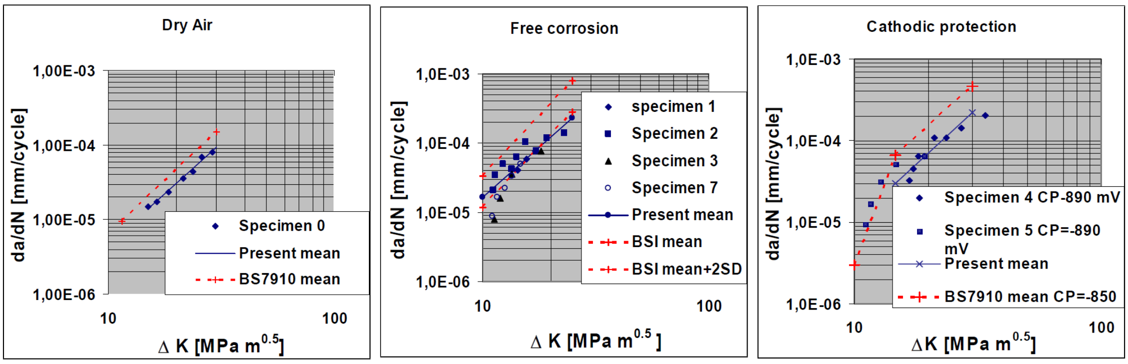

(a) [Lassen et al., 2005, p.3] *(b) [Lassen et al., 2005, p.4]* *(c) [Lassen et al., 2005, p.5]*

Figure 3.8: Crack growth test results. [Lassen et al., 2005]

Further testing was therefore done with specimen 7, loading it with three different blocks of ΔK; 4MPa$\sqrt{m}$, 6MPa$\sqrt{m}$ and 8.5MPa$\sqrt{m}$. Only the block with 8.5MPa$\sqrt{m}$ loading showed any crack growth. This observation means that the SIF threshold value for the free corrosion of R4S steel may be as high as 6MPa$\sqrt{m}$. When the crack growth measurements from the ACPD of specimen 7 were extrapolated, a threshold of 4.5 MPa$\sqrt{m}$ was found. This shows a relatively good agreement between the replica method results and the ACPD. On basis of these results, a threshold value of 5MPa$\sqrt{m}$ was suggested [Lassen et al., 2005, p.4].

The parameters for the regressed lines, as well as the ones given in BS7910, are given in 3.5. The lines denoted as *Lassen et. al* are the lines generated by regression, when the slope of the curve, m, is allowed to vary freely. *Forced m* on the other hand, is the regression conducted with a forced slope of m equals 3, as specified in [DNV-OS-E301, dnv]

With regards to the cathodically protected chain specimens, an unusual result was found, as there was indication of crack arrest and crack closure for the specimens with highest cathodic

Table 3.5: Growth Parameters, units in m and MPa. [Lassen et al., 2005, p.4,5,6]

Dry Air		
	m	C
Lassen et. al	2.70	$9.5 \cdot 10^{-12}$
BSI7910	2.88	$8.3 \cdot 10^{-12}$
Free Corrosion		
Lassen et. al	2.88	$21.4 \cdot 10^{-12}$
Forced m	3.0	$17.5 \cdot 10^{-12}$
BSI 7910	3.44	$4.0 \cdot 10^{-12}$
Cathodic Protection		
Lassen et. al	2.81	$15.8 \cdot 10^{-12}$
Forced m	3.0	$12.0 \cdot 10^{-12}$
BSI7910(*)	2.67	$52 \cdot 10^{-12}$
Recommended	3.0	$17.5 \cdot 10^{-}12$

protection. This is contrary to the usual assumption that high strength steel will be weakened by hydrogen embrittlement when the cathodic protection increases.[Lassen et al., 2005, p.5]

Microscopy of the fatigue surfaces was also conducted. The striations were clear for the dry air specimens, but they were less pronounced for the tests in sea water. There was some indication of secondary cracking. These cracks were oriented lateral to the main direction of crack propagation.

The mean crack growth rates under the different conditions are summarized in Figure 3.9.

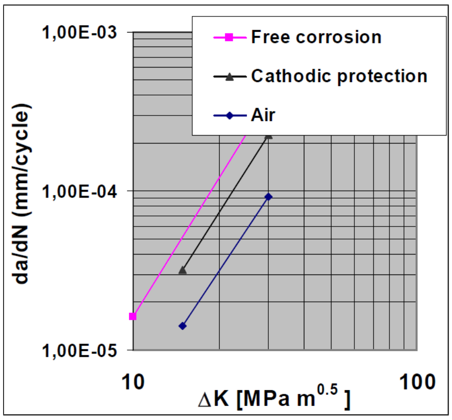

Figure 3.9: Mean crack growth rates for different conditions. [Lassen et al., 2005, p.6]

Chapter 4

Fatigue Life Model

The fatigue life of a chain in sea water is influenced by a large variety of factors, primarily comprising of different sorts of corrosion and fatigue damage. In the model that is to be proposed, it is therefore important to ensure that these effects are accounted for in a reasonable manner, without making the model too complex. The following sections will describe which effects are included in the model.

4.1 Fatigue Damage

The proposed model is based on fracture mechanics. The fatigue crack propagation is modelled by calculating the stress intensity factor at different crack lengths, and applying Paris' Law, Eq. 3.20, to determine the amount of cycles required to propagate the crack from an initial to a final depth. This is done by finding the geometry function for the SIF, and performing a numerical integration from an initial to a final crack depth.

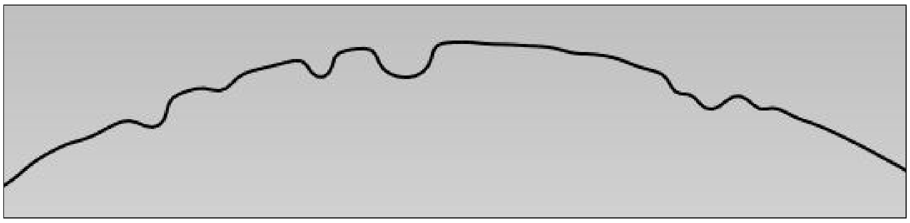

(a) Extracted profile from corrosion on chain specimen.

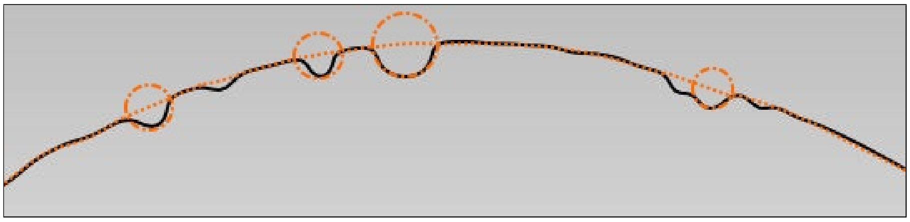

(b) Overlapping idealized circular shapes.

4.2 Corrosion

The effect of corrosion can be accounted for in three ways:

- Reduce the general cross section area of the chain.

- Use crack growth parameters found while testing in corrosive environments, including threshold ΔK for crack closure.
- Introducing corrosion pits to the surface of the model. Figure 4.1b.

The reduction of cross section area is ignored in the model. This is due to it being complicated to model, as it is dependent on time, as well as the limited effect it is assumed to have on the crack growth itself. Corrosive crack growth parameters are used in conjunction with Paris' Law, and the crack closure is also included for some of the calculations by reducing the ΔK, as described in Section 3.3.3.

Multiple ways to include the effect of corrosion pits have been proposed. A pit can be assumed to be an elliptical crack [Sirevaag, 2015], an elliptical notch [Garbatov et al., 2014], or, as [Wei, 2000, p.11], a hemispherical notch. Alexander Hoel performed a scan of the crown of a chain link, and from these scans, a surface profile was extracted, Figure 4.1a. Considering the profile, the pits were redrawn with orange circles illustrating the approximated pit shape, Figure 4.1b, for hemispherical notches.

4.3 Mechanical Wear

Mechanical wear between the two chain links cause a local reduction of cross sectional area in the crown. Evy Bjørnsen performed stress analyses where a 13.2% reduction of cross sectional area was modelled [Bjørnsen, 2014, p.109]. She concludes that the reduction in wear can have a positive effect on the chain link, as it increases the contact area between the chain links, which in turn reduces the bending stresses in the crown [Bjørnsen, 2014, p.110]. The effects of area reduction beyond 13.2% is not investigated. On the basis of Evy's analyses, it was decided to ignore the effect of wear in the proposed model.

4.4 Effect of Crack Origin

The effect of where the crack originates is not known, and three different cases are therefore modelled in order to estimate how it affects the fatigue life. The three different cases are listed below, and shown in Figure 4.2:

1. Crack initiating from bottom of notch.
2. Crack initiating from notch root at the surface.
3. Crack encompassing the notch.

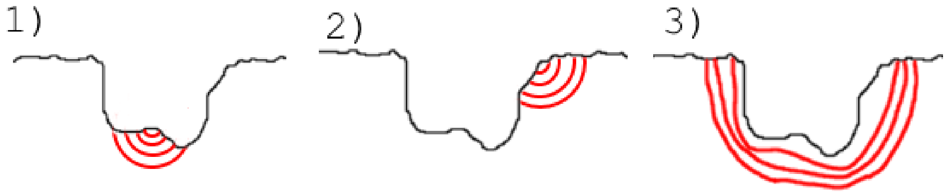

Figure 4.2: Origin locations on pit.

Three hypotheses were made in order to describe the crack growth through the crown of the chain link. The hypotheses are divided into an initial, transition and stable growth regime. The gray area in the figures is the notch.

Hypothesis 1 The bottom crack grows until it becomes a fully developed circular surface crack with origin at the surface of the specimen. After exiting the transition region, the crack front is free to develop in the stable growth regime. Figure 4.3.

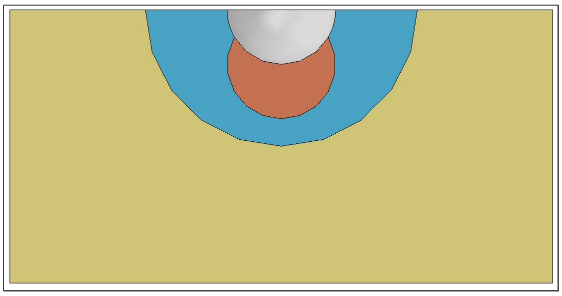

Figure 4.3: Hypothesis 1 growth. Red zone is the initial growth regime, blue is the transition regime and bright yellow is the stable growth regime

Hypothesis 2 The side crack grows until it reaches the same depth as the pit, and it then grows sideways until it encompasses the pit and it can be considered an elliptical surface crack of ratio (a/b)=0.5. It continues growing in an elliptical shape until it exits the transition region. After this the crack front is free to develop in the stable growth regime. Figure 4.4.

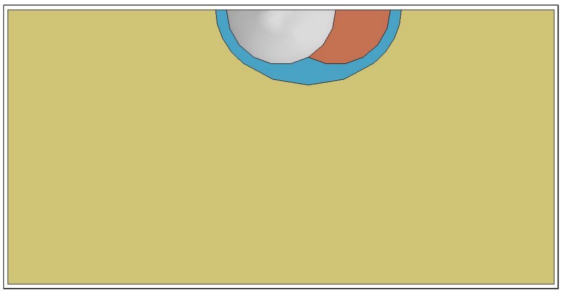

Figure 4.4: Hypothesis 2 growth. Red zone is the initial growth regime, blue is the transition regime and bright yellow is the stable growth regime

Hypothesis 3 The encompassing crack continues growing as a circular crack until it exits the transition region. After exiting, the crack front is free to develop in the stable growth regime. Figure 4.5.

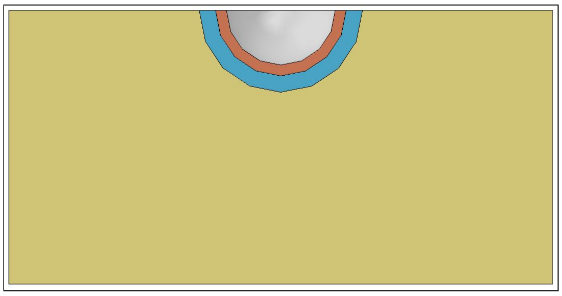

Figure 4.5: Hypothesis 3 growth. Red zone is the initial growth regime, blue is the transition regime and bright yellow is the stable growth regime

4.5 Effect of Crack Front Shape

There are handbook solutions for rods with elliptical surface cracks, and one such solution was presented by Shin and Cai [Shin and Cai, 2004]. When considering the deepest point of the crack, it is readily seen from Figure A.5 that the geometry factor is higher for an elliptical crack, than a circular crack. The difference becomes increasingly pronounced as the crack propagates through the chain. Assuming the correct crack front shape is therefore important for the estimation of life of the component. For the rest of the study, the crack nomenclature described in Figure 3.5b will be used, and the ratio (a/b) shall be referred to as the crack ratio.

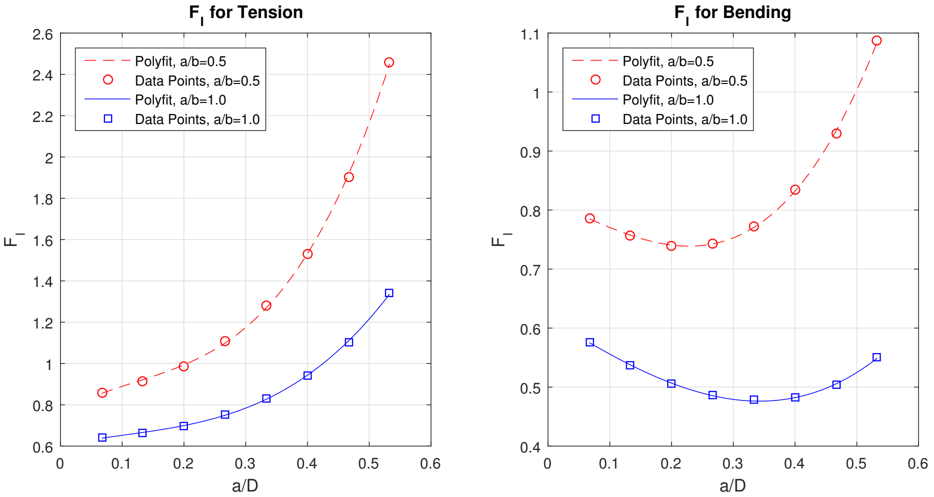

Figure 4.6: Geometry factors for a rod in tension and bending, [Shin and Cai, 2004, p.241]

As mentioned in Section 3.3.3, the crack front shape is related to the type of loading, crack growth exponential parameter m of Paris-Erdogan's law, and the initial crack aspect ratio. The chain link is subject to a high degree of bending in the crown, and in order to accurately model the crack front shape of a crack in a chain link, the bending crack front shape solutions by Couroneau and Royer [1998] were used. Two different cases were modelled, one with an initial crack ratio of 1, and another with a ratio of 0.5. The development of the shape for these two cases is seen in Figure 4.7. How these functions were derived is explained in Appendix B. They are, however, only valid when (a/D) varies from 0.1 to 0.5, due to Couroneau and Royer [1998] not performing analyses for shorter or longer crack lengths. The hypotheses that were presented for the crack growth in the initial regime assume further crack growth to be circular or elliptic. In order to have the initial and stable regime be as consistent as possible, and since no data is available to improve the assumption, it is assumed that any crack shorter than 0.1 maintains a constant aspect ratio, as is readily seen in Figure 4.7.

4.6 Material Model and Crack Growth Parameters

Chain links are made of high strength steel of varying quality, as described in Section 2.2.4. The mooring systems that are being considered, are designed for high cycle fatigue, which means that they will experience mostly low levels of stress throughout their lifetime. The presence of plasticity should therefore be limited, and a linear elastic material model was assumed. Lassen et al. recommend the the crack growth parameters in Table 4.1, shown together with the material properties used [Lassen et al., 2005, p.9].

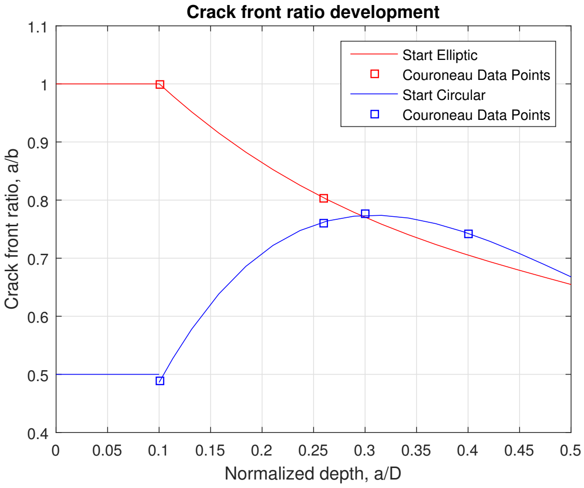

Figure 4.7: Modified crack front development, see Appendix B.

Table 4.1: Linear elastic material properties and crack growth parameters.

Property	**Value**
Young's Modulus, E	210 000MPa
Poisson's Ratio, ν	0.3
m	3.0
C	$17.5 \cdot 10^{-12}$

4.7 Model Overview

In order to include all the effects described above, the fatigue model was divided into two parts; a local and a global model, Figure 4.8. The local model will consist of a cube with an idealized corrosion pit, and will model the effect of said pit on SIF and fatigue life, and how it interacts with where the cracks initiate. The local model will model the initial crack growth of the growth hypotheses. The global model will consider the crack growth after it enters the stable growth regime. This will be done by modelling the crack propagation through the chain link from two different initial crack ratios as described in Section 4.5. The transition regime is not modelled, and will be estimated by curve fitting the results from the local and global analyses. The resulting model will be referred to as the combined model. The following chapters will describe the global and local model in further detail.

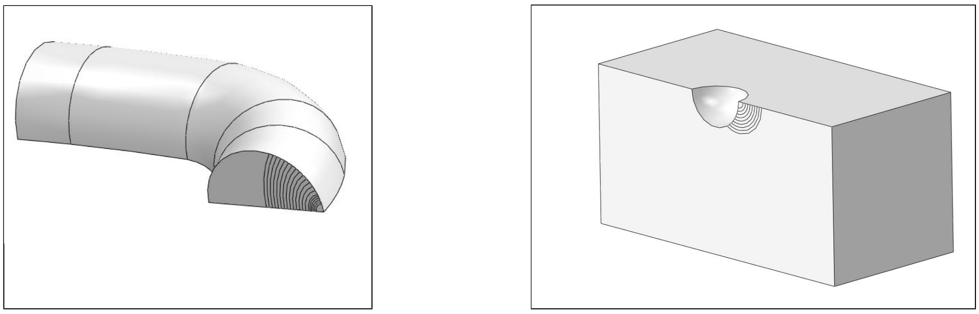

(a) Global model, the elliptical lines indicating different crack depths.

(b) Local model, the elliptical lines indicating different crack depths.

Figure 4.8: Global and local model.

Chapter 5

Local Modelling

In order to model the effect of corrosion pitting, cubic finite element models with an idealized semi-circular notch were made. Cracks were inserted at different locations in the model, for a total of three cracked configurations as seen in Figure 5.1.

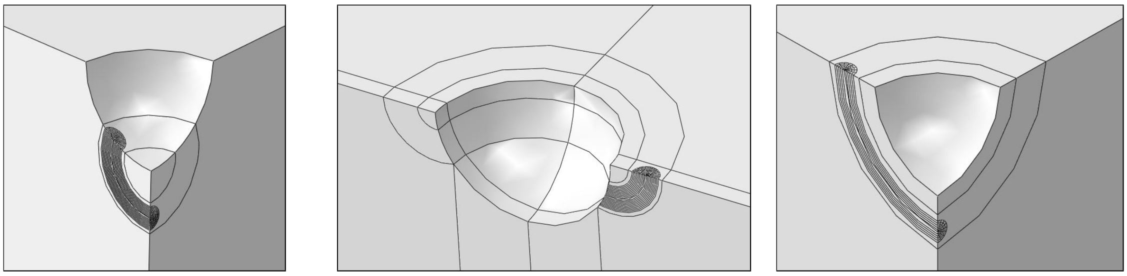

(a) Crack growing from the bottom of the notch. *(b) Crack growing from the side of the notch.* *(c) Crack encompassing the notch.*

Figure 5.1: Crack configurations.

The cracks in the models were propagated by creating new models with different crack depths. As the model is assumed to be linear elastic, it is history independent, and the crack propagation can therefore successfully be modelled as individual analyses at different crack depths. The crack front is assumed to maintain a semi-circular shape throughout the propagation phase. The models were subject to two load cases, pure tension and pure bending, both at 100MPa. A summary of the number of models and crack increments is seen in Table 5.1.

Table 5.1: Summary of the local models, note that there are two models per increment, due to the two load cases.

Model	**Initial Crack Depth [mm]**	**Incremental Growth [mm]**	**Final Depth [mm]**	**Nr. Models**
Bottom Crack	0.4	0.1	1.0	14
Side Crack	0.2	0.1	1.0	18
Enclosed Crack	1.3	0.1	2.0	16

In order to ensure that the cubes were large enough that the finite width would not interfere with the results, a study was performed with varying crack and cube depth ratios with a circular surface crack. The study is shown in Appendix D.1. The results indicate that the effect of the boundary can be neglected, as long as the ratio between crack and cube depth does not exceed 0.1.

5.1 Bottom Cracked Model

The bottom cracked model is symmetric about two planes, and models a crack growing from the bottom of the notch with a strict circular shape, until a final depth of 1mm. The model uses submodelling to reduce the computational power required in order to have a satisfactory mesh refinement around the crack.

5.1.1 Geometry

The geometry of the models is seen in Figure 5.4. The different crack models have varying crack length, and the concentric circles from the bottom of the notch show the different crack depths modelled, Figure 5.2b, starting from 0.4mm and ending with 1.0mm, as seen in Table 5.1.

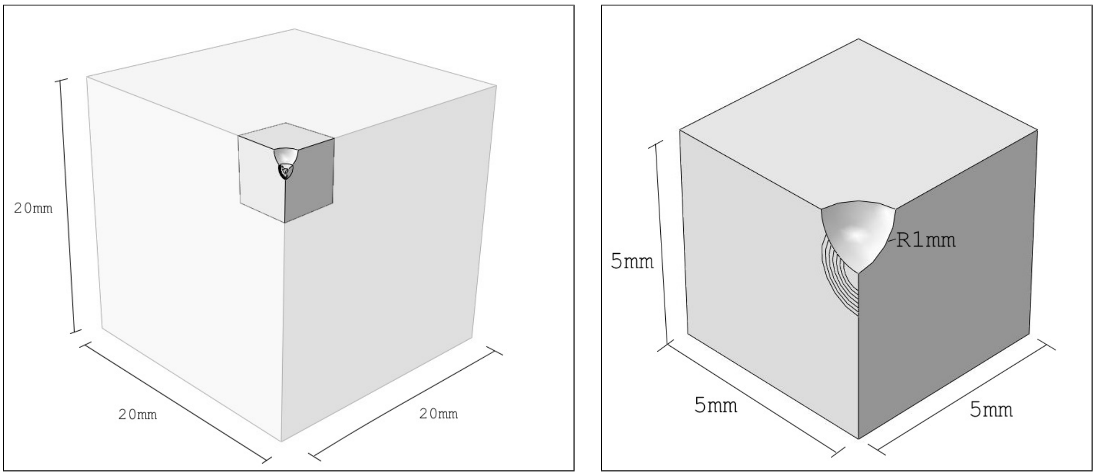

(a) Reference model.

(b) Submodel of the bottom crack.

Figure 5.2: Bottom cracked geometry.

5.1.2 Mesh

The elements used are second order 20 node cubic elements, C3D20 in ABAQUS. Cubic elements are required for crack analyses in ABAQUS. Second order elements provide an increased accuracy, and allows the node at the crack tip to be collapsed, and have the midside nodes moved. They could not be moved to the quarter node position however, due to problems with the ABAQUS meshing algorithm, which generated highly irregular element shapes at the crack tip. A figure of the irregular mesh is seen in Appendix D.2.

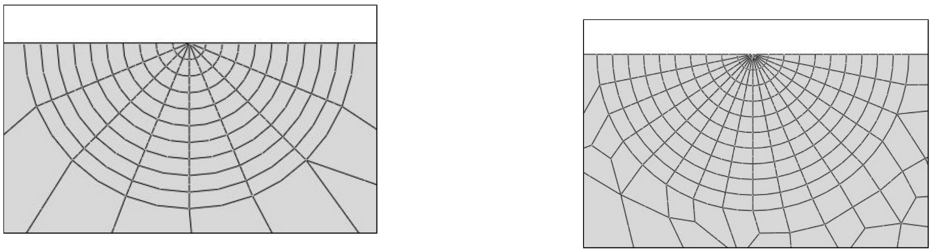

(a) Profile view of the reference model spider web mesh.

(b) Profile view of the submodel spider web mesh.

Figure 5.3: Spider web mesh profile.

The global element size in the reference model was 1.0, while the submodel had a global seed size of 0.1. The spider web mesh was generated by cutting the notch with a shell model with the finished mesh partition. The mesh design had an element depth of 10 elements for both models, but the angular element number is 8 for the reference model, and 16 for the submodel, as seen in Figure 5.3.

5.1.3 Boundary Conditions and Loading

The reference model has two planes of symmetry, and symmetry boundary conditions are applied to these surfaces, as seen in Figure 5.5c. The back faces are loaded with an evenly distributed surface traction of 100MPa in the X-direction in the first load case, and a linearly varying bending load in the second case. The analytical function used to replicate the bending load is seen in Eq. 3.22a.

$$S = \left(\frac{Y-10}{10}\right) \cdot S_{max} \tag{3.22a}$$

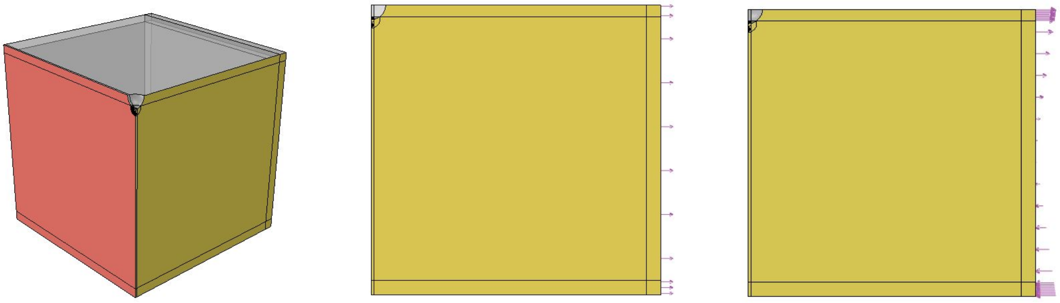

(a) Cube with boundary conditions, red is z-symmetry, and yellow is x-symmetry.

(b) Side view showing the tensional load distribution, it is applied to the whole suface.

(c) Side view showing the bending load distribution, it is applied to the whole suface.

Figure 5.4: Bottom cracked geometry.

The submodel has three of it's faces inherit the x,y and z displacements found in the corresponding location in the reference model. The top surface is free, while symmetry is applied to the last two surfaces, as seen in Figure 5.5.

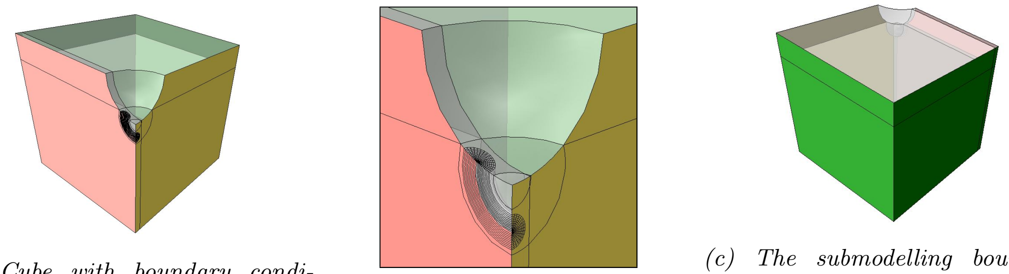

(a) Cube with boundary conditions, red is z-symmetry, and yellow is x-symmetry.

(b) Close-up of the crack and notch region.

(c) The submodelling boundary conditions. The bottom face, which is not visible, also has submodelling boundary condition.

Figure 5.5: Submodel boundary conditions

5.2 Side Cracked Model

The side cracked model, investigates the growth of a crack from the root of a notch. The crack grows in a strictly circular shape. The model also utilizes submodelling.

5.2.1 Geometry

The geometry of the side cracked model is seen in Figure 5.6. The concentric rings show the different crack depths that were modelled.

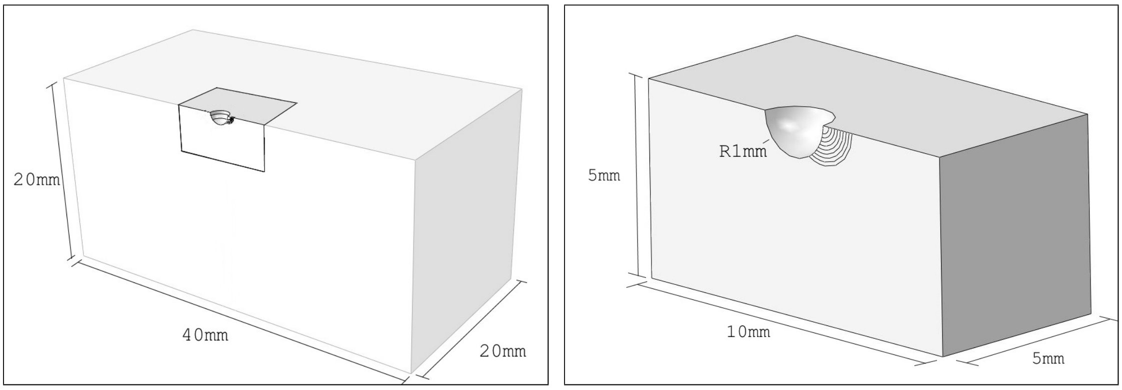

(a) Reference model.

(b) Submodel of the side crack.

Figure 5.6: Bottom cracked geometry.

5.2.2 Mesh

The global mesh size for the reference and submodel were 1.0 and 0.1 respectively. The same spider mesh profile as seen in Figure 5.3 was used for both the reference and submodel.

5.2.3 Boundary Conditions and Loading

The loading on the reference model is the same as with the bottom cracked model. The boundary conditions are slightly altered, as there is only one plane of symmetry.

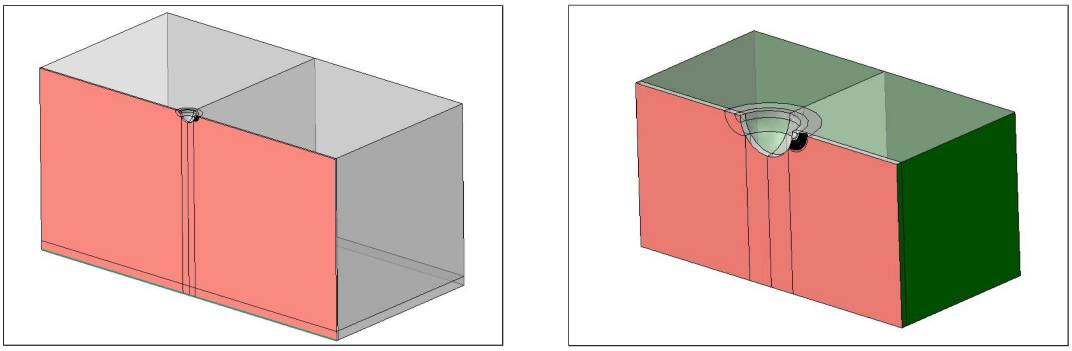

(a) Reference model boundary conditions. The loading is equivalent to the bottom crack.

(b) Submodel boundary conditions. Bottom also has submodel BC, but it is not visible.

Figure 5.7: Bottom cracked boundary conditions.

5.3 Enclosed Crack Model

The enclosed crack model investigates the effect of the notch on a circular surface crack. The crack grows in a strictly circular shape. The model also utilizes submodelling.

5.3.1 Geometry

The enclosed crack model is symmetric about two planes. The crack depths modelled are seen as concentric circles in Figure 5.8.

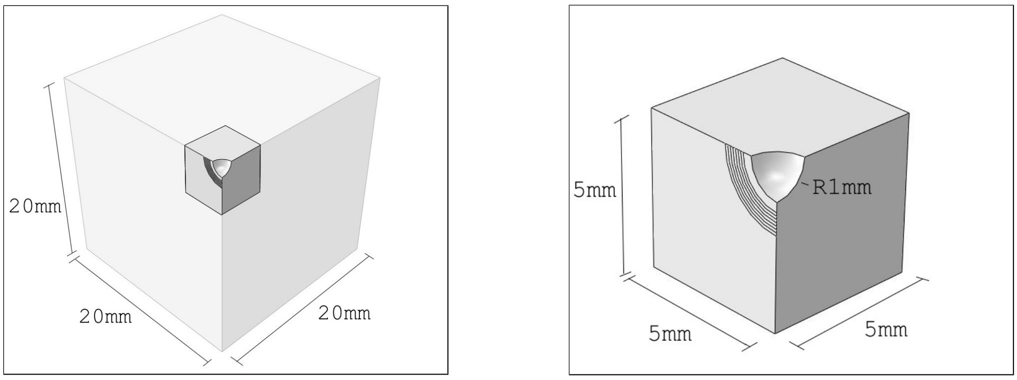

(a) Reference model. *(b) Submodel of the bottom crack.*

Figure 5.8: Enclosed cracked geometry.

5.3.2 Mesh

The global seed size is 1.0 and 0.1 for the reference and submodel respectively. The same spider web configuration as used in the bottom cracked model is used, Figure 5.3.

5.3.3 Boundary Conditions and Loading

The loading on the reference model is the same as with the bottom cracked model. The boundary conditions are also the same, as there is a double symmetry, for both the reference and submodel. The boundary conditions are seen in Figure 5.9

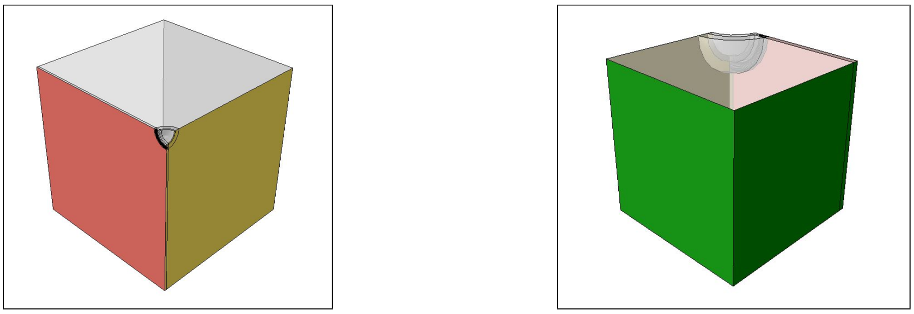

(a) Reference model boundary conditions. The loading is equivalent to the bottom crack. *(b) Submodel boundary conditions. Bottom also has submodel BC, but it is not visible.*

Figure 5.9: Bottom cracked geometry.

Chapter 6

Global Model

The global model considers the crack growth through the chain link after the crack has reached an appreciable size. Two different growth situations were modelled, one starting with a circular crack, and another with an elliptical crack ratio of (a/b=0.5). This is done in order to see the difference in the result from the crack growth hypotheses on the local scale.

The three dimensional model models a contact problem between two chains, where one has a crack in the crown. The crack is propagated by changing the length of the crack and remeshing the component. The shape of the crack front varies in order to adhere to the results by the research published in [Couroneau and Royer, 1998], and the crack ratio as seen in Figure 4.7.

As three dimensional simulations are costly, two simplified methods were investigated. One was proposed by Lassen [Lassen et al., 2005] , which suggests combining handbook solutions for surface cracks in rods with the stress analyses of the chain in order to estimate the stress intensity factor of a surface crack in the chain. The second method, proposed by the author, bases itself on performing a simplified two dimensional crack analysis, and later adjusting the stress intensity factor by multiplying it with the geometry factor for an elliptical crack shape. These methods were tested and verified, and the procedure is described in Appendix B.

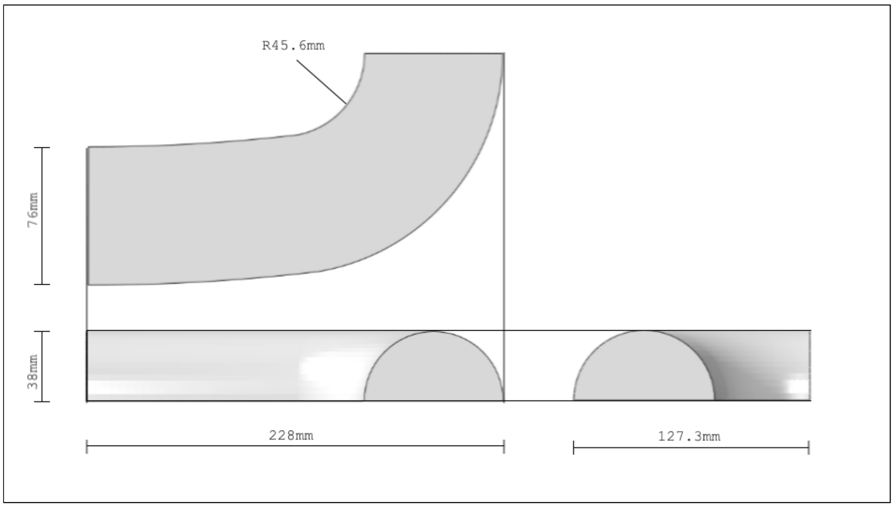

Figure 6.1: Chain link geometries.

Geometry

The chain geometry is seen in Figure A.2. The cross sectional diameter was set to 76mm, and the geometries follow the specifications set in Figure 2.7. The links are symmetric along three planes, and only an eight of the full chain was therefore modelled. They are 3D deformable solids, and were made by sweeping a semi-circular sketch along a spline path.

The development of the crack front in the two different cases is seen in Figure 6.2.

(a) Crack front development, when origin is circular. *(b) Crack front development, when origin has crack ratio (a/b)=0.5.*

Figure 6.2: Crack front development in chain.

Interaction

The model includes a contact between the two chains. A surface to surface discretization was used. Nodes from the slave surface are not allowed to penetrate between two master nodes, and the finely meshed surface was therefore chosen as the slave, while the coarser was set as master.

The contact properties consists of a tangential and a normal setting. The tangential behaviour was defined using the penalty formulation with isotropic directionality. As the value of the tangential frictional coefficient had little effect on the results of the stress analyses [Bjørnsen, 2014, p.84], the same value as was propsed by Evy Bjørnsen was used. The normal behavior was set as hard, in order to minimize penetration.

The contact surfaces were chosen large enough to ensure that no amount of deformation would cause an area not defined for contact to interact with the contact area. The contact surfaces are seen in Figure 6.3.

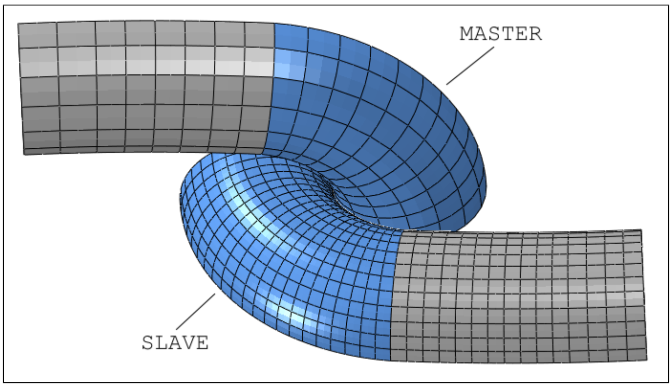

Figure 6.3: Contact Surfaces, Evy model.

Mesh

The mesh uses a global element size of 5 and 8 respectively for the slave and master chain links. The mesh has been changed locally in the crack region, where a spider web mesh has been implemented, Figure 6.4b, as with the local model [Anderson, 2007, p.574]. The elements around the crack tip are cubic elements that have been collapsed onto one node, with midside nodes moved to the quarter point along the edge. Crack tip elements from the surface are seen in Figure 6.4a.

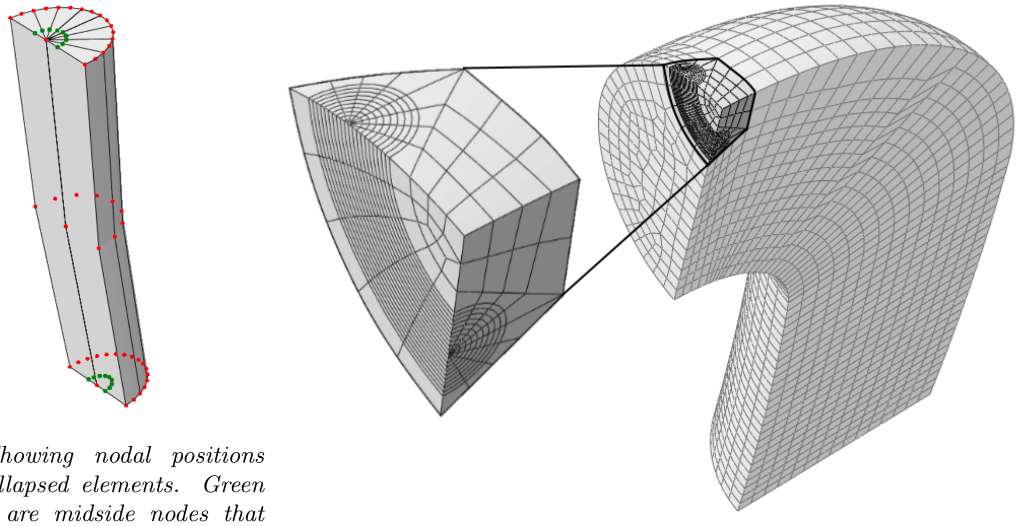

(a) Showing nodal positions for collapsed elements. Green nodes are midside nodes that were moved.

(b) Crack mesh geometry, 14mm circular crack, Evy

Figure 6.4: The mesh of the slave chain with a crack.

Boundary Conditions and Loading

The three symmetry planes were assignedas seen in Figure 6.5. The master link is loaded with a constant surface traction, and the top surface is hinged, so that it cannot move in XZ-plane.

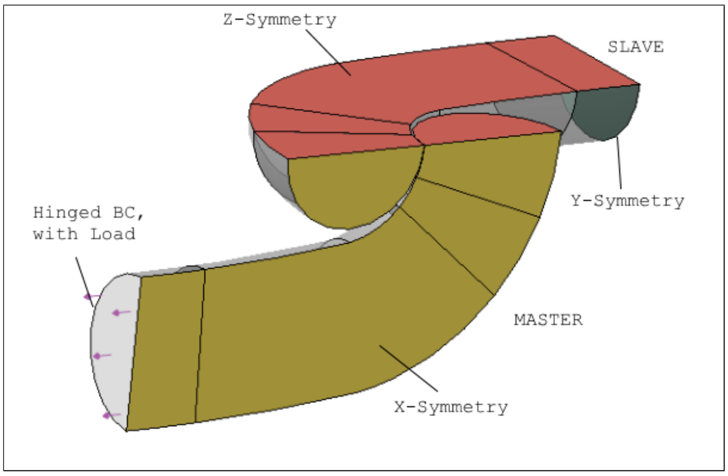

Figure 6.5: The load and boundary conditions. Red iz Z-symmetry, yellow X-symmetry, dark green Y-symmetry, and white, hinged. Load is seen as purple arrows.

Chapter 7

Results and Discussion

The results for the local model will be presented first, followed by the global model. In the end, the results will be combined to create a full crack growth model.

The stress intensity factors from the analyses were normalized by Eq. 3.22a:

$$K_0 = \frac{K_I}{S\sqrt{\pi a}} \tag{3.22a}$$

Where S is the far field loading applied to the system. For the global model, this is the load applied to the master chain link, while it for the local model is the tensile stress and maximum bending stress applied.

7.1 Local SIF Results

The stress intensity factor has been normalized against the far field loading of the specimen. It was proposed in Section 4.4, that the side crack would evolve into an elliptical crack, while the bottom crack would become equivalent to a circular surface crack encompassing the pit. In order to capture these trends, the Newman-Raju solutions [Newman and Raju, 1981] for elliptical surface cracks in plate for the two crack ratios 0.5 and 1.0 were plotted in the figure. As the bottom crack evolves into an encompassing circular surface crack, the crack tip distance from the surface was used as the x-axis of the plot, as described in Eq. 3.22b for the bottom crack. For the encompassing and side crack, the crack tip distance from the surface is equivalent to the crack depth.

$$a_s = a_{crack} + r_{pit} \tag{3.22b}$$

Where a_{crack} is the depth of the crack from it's point of origin, and r_{pit} is the radius of the pit. It should be noted that the normalization employs the crack depth a_{crack} for all configurations.

7.1.1 Transformation to the Global Case

As an approximation to the global case, a load equivalent to the loading in the upper 20mm of the chain link was applied to the specimen, as illustrated in Figure 7.2, by superposition of the previous solutions. Sampling the stress distribution at the surface of the chain σ_{76}, and 20mm below the surface σ_{56} from Figure A.3, one can calculate the tensile and bending contribution factors as:

$$C_t = \left(\frac{\sigma_{76} + \sigma_{56}}{2}\right) \cdot \frac{1}{S} = 3.5 \tag{3.22ca}$$

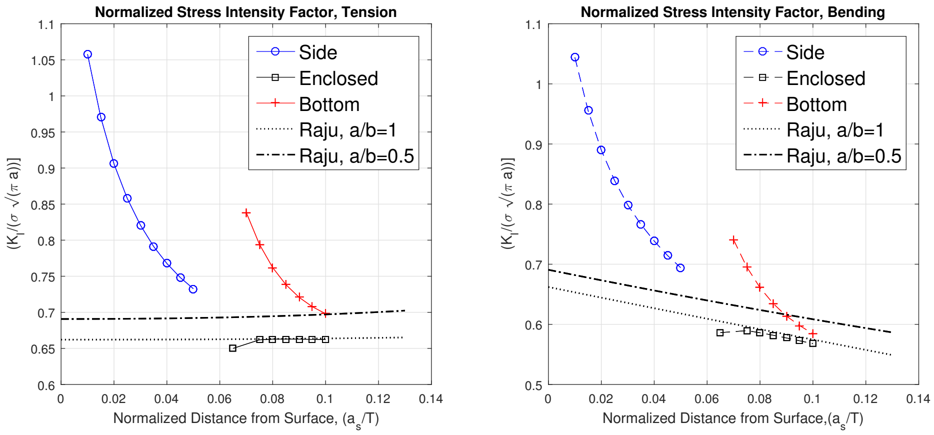

Figure 7.1: Normalized stress intensity factors for different crack configurations around a pit.

$$C_b = \left(\sigma_{76} - \frac{\sigma_{76} + \sigma_{56}}{2}\right) \cdot \frac{1}{S} = 0.8 \tag{3.22cb}$$

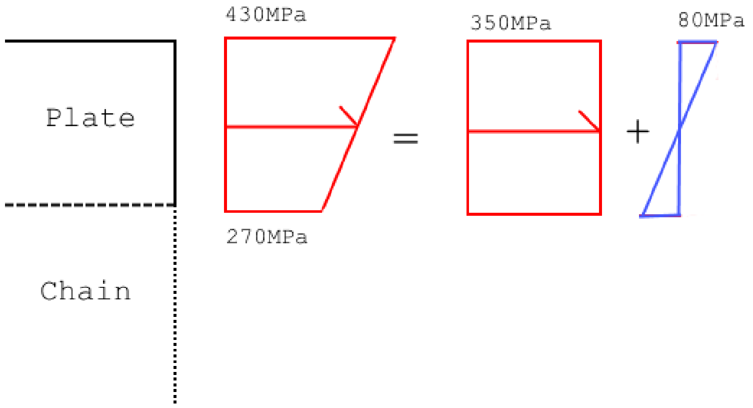

Figure 7.2: Decomposition of load in crown of chain to the local model. σ_{76} *= 430MPa, and* σ_{56} *= 270MPa*

The corrected geometry factor is seen in Figure 7.3. Note, that the true crack depth is used in the plot.

7.1.2 Review of Local Results

It is seen shown that the geometry factor for a crack originating in the side of a pit is higher than one originating in the bottom. As this is the case for both bending and tension, the same results are seen with the global loading approximation in Figure 7.3. It follows from this result that the SIF also is higher. In Section 3.2.1, the Kondo criteria for the corrosion pit to crack transition which was further developed by Wei [2000], was introduced. As is seen from Eq. 3.3, the transition from corrosion pit to crack requires the stress intensity factor for the future crack to be larger than the threshold value. This finding suggests that the cracks should initiate in the side of the pit, as suggested in Hypothesis 2, for both a plate (local model) and the combined global model.

As was just concluded, the geometry factor is highest for a crack growing with it's origin from the side of the pit.

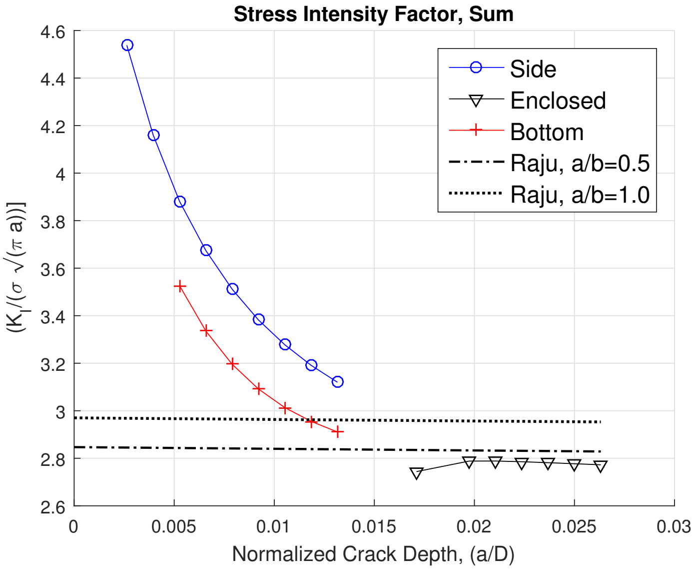

Figure 7.3: Local geometry function, corrected for global loading.

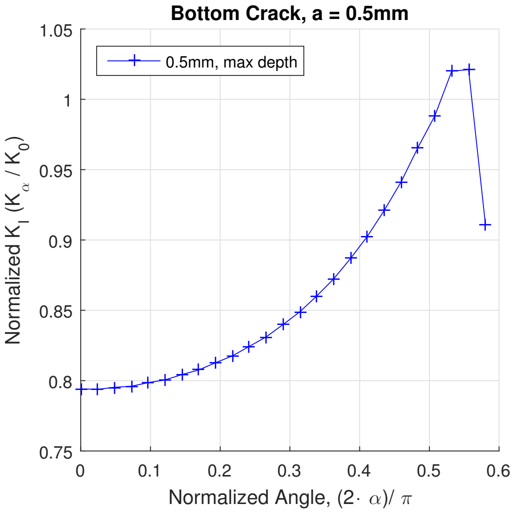

Figure 7.4: Normalized stress intensity factor along the crack front of a bottom crack. The normalized angle is zero at the bottom of the crack.

The crack front shape of all the solutions is forced to be circular. As can be seen from Figure 7.4, the value of the geometry function is much higher near the free surface than at the bottom of the crack. At the surface, the function tends to zero, but this is due to how ABAQUS calculates the contour integral as a piecewise average along the crack front. As discussed in Section 3.3.2, the contour integral will become zero at a free surface since the singularity is not $r^{0.5}$. This combined with the piecewise average contour integral calculation, causes a local zero at the surface. As the stress intensity factor is not constant, it safe to assume that the crack front does, in fact, not stay circular, but will change shape. It will grow into an elliptical shape in the beginning, but exactly how this will occur is outside the scope of this study. Suffice to say, that there is an uncertainty related to the accuracy of the local model results, which is not easily quantifiable.

7.2 Global SIF Results

The solutions were again normalized as in Eq. 3.22a. The trends are as expected, the crack that starts elliptical has a much higher normalized stress intensity factor than the crack that starts circular. The crack that does not develop, but stays circular, has the lowest normalized SIF.

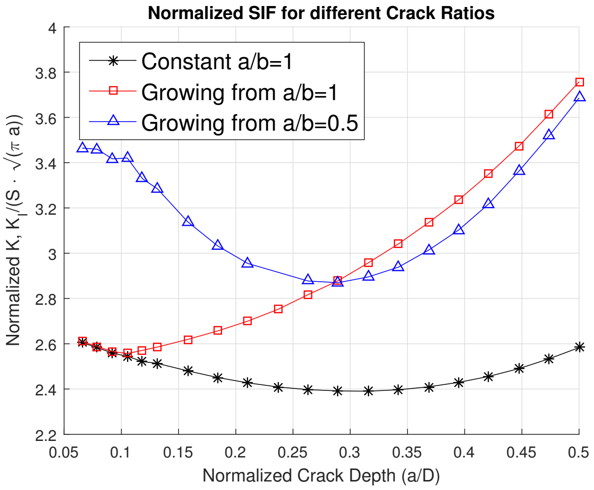

Figure 7.5: Normalized stress intensity factors for different crack configurations around a pit.

7.2.1 Review of Global Results

The global model assumes that the crack front shape stays similar to the one observed for a rod in bending in [Couroneau and Royer, 1998]. There is currently no better data available, and it is therefore not possible to prove or disprove the accuracy of this assumption. Especially the region where the crack is shorter than 0.1 (a/D) requires further studies. In order to obtain better results, fractography should be performed on chains that have been subject to fatigue testing in order to find a better estimate for the crack front shape. Alternatively, a more advanced fracture mechanic

An indication of the quality of the calculations can be obtained through the use of handbook solutions. Figure 7.6a and Figure 7.6b shows the calculated SIF bounded by the solutions from Shin and Cai [2004]. The bounds were picked from Figure 4.7. The solutions by Shin and Cai [2004] are only available for increments of 0.1, and the bounds are therefore not perfect. Also, Shin used rods, and not chains, which causes his solutions to have a higher SIF as the crack goes deeper due to the linearization approximation showed in Appendix B. From the aforementioned figures, it is seen that the solutions behave as expected, and are reasonable.

7.3 Combined SIF Results

The results from the local and global model were combined in order to create a model for the complete crack growth through the chain link. The data points from the analyses are seen in Figure 7.7a. The proposed hypotheses were used in order to combine the results. A modification of the second hypothesis was also included. This modified hypothesis, assumes that the side crack will not develop into an elliptical crack, but instead continue as a circular crack until it reaches a certain depth, here set as where the global model takes over. The modified hypothesis will from now on be referred to as hypothesis 2M, or H2M.

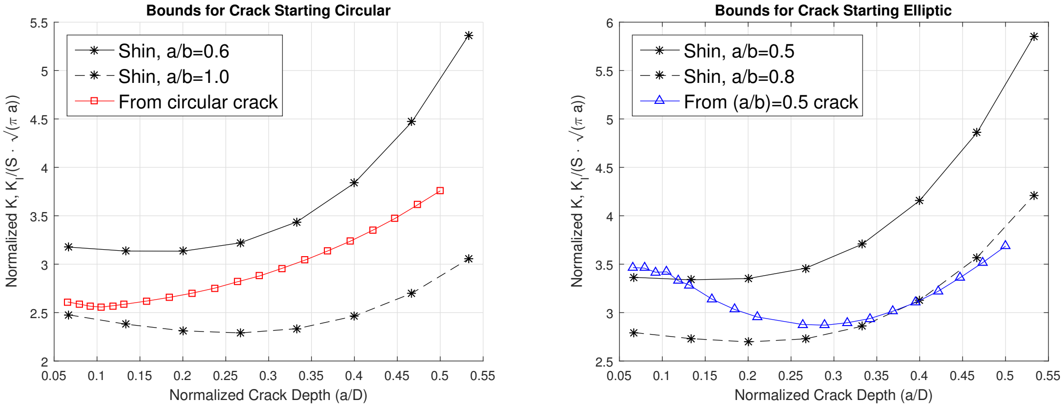

(a) SIF Solution for crack starting circular, bounded by the handbook solutions from Shin and Cai [2004].

(b) SIF Solution for crack starting elliptic, bounded by the handbook solutions from Shin and Cai [2004].

Curve fitting was performed between the global and local analysis. The trends for hypothesis 1,2M and 3, as seen in Figure 7.7c, Figure 7.7d and Figure 7.7e respectively , seem to indicate a growth into the proposed circular shape, and the curve fits are therefore quite good. Hypothesis 2 does not show a good correlation. In order to model this hypothesis, it was chosen to consider the last 5 points of the local analysis as outliers. The outliers are shown together with the fitted function in Figure 7.7b. The equations resulting from the curve fitting are given in Appendix C.

7.3.1 Review of Combined SIF Results

The SIF results from the local and global model individually show good correlation with their respective handbook solutions. The challenge with the combined model is the transition region. How the crack develops according to the different hypotheses is not modelled, and could turn out to be vastly different from what is being assumed. This is very clear with the lack of consistency between the local and global results for the side crack. The following explanation is proposed for the discrepancy:

Figure 7.8 shows two surface cracks on a plate and a rod with an intersecting origin. For a plate, the elliptic and the circular surface cracks intersect the free surface at the same horizontal level. The crack front is long, and the stress can be redistributed along the whole front. For the rod, however, the local stress is amplified not only by the elliptic crack being wider than the circular, but also the loss of material at the sides. The result being even more stress being redistributed along the front of the crack, which is now shorter.

The handbook solutions by Shin and Cai [2004], for surface cracks in rods, and Newman and Raju [1981], for surface cracks in plates, were used to compare the relative geometry factor for cracks of ratio a/b=0.5, F_E, and a/b=1.0, F_C for both bending and tension. It is seen, from Figure 7.9 that there is a much larger difference between the elliptical and circular cracks for a rod in both tension and bending than for the equivalent in a plate. This holds for even very short cracks. This result supports the explanation proposed above, that the idealization of the surface as a horizontal plate does not hold for the chain link.

7.4 Life Estimation

By employing the procedure described in Section 3.4.2, a program was written in MATLAB which integrates Eq. 3.19, in order to calculate the life of the components depending on the initial flaw size present. The program was run once for each model; local, global and combined,

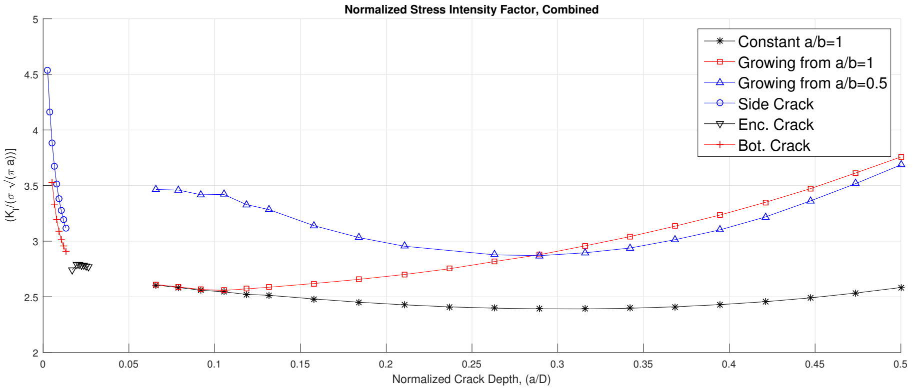

(a) Full view of data points from analyses.

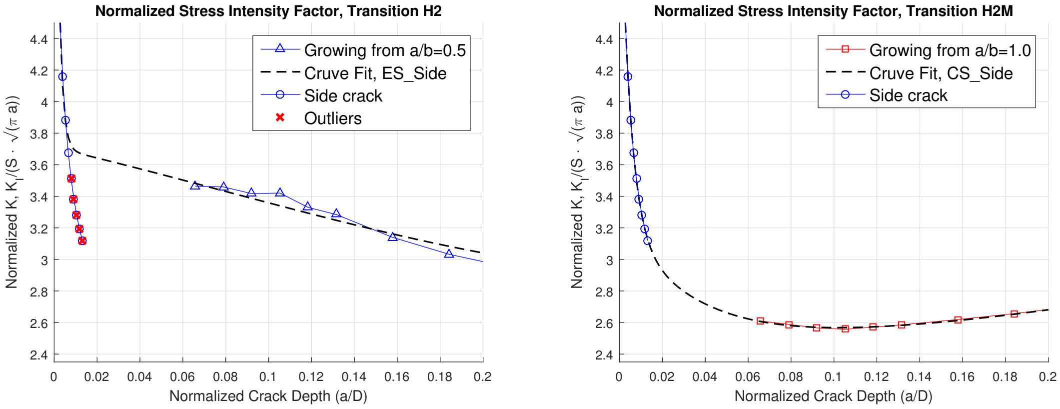

(b) Curve fitting for Hypothesis 2.

(c) Curve fitting for modified Hypothesis 2.

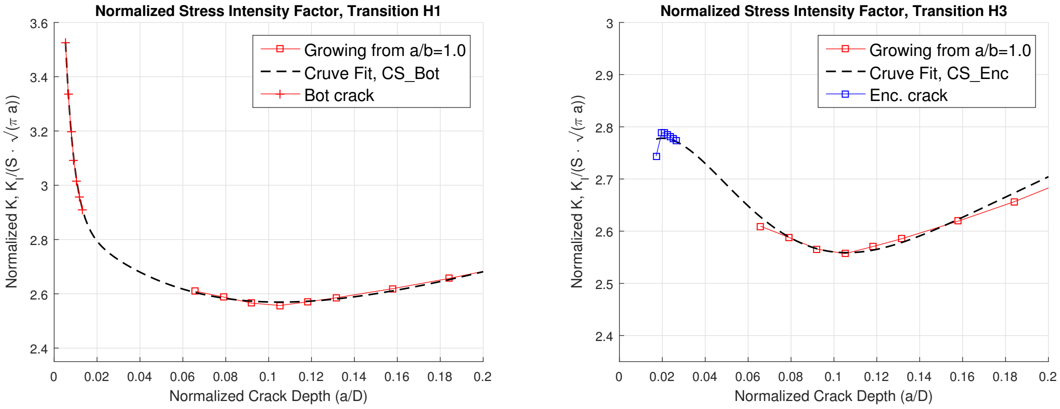

(d) Curve fitting for Hypothesis 1.

(e) Curve fitting for Hypothesis 3.

with the flaw dimensions as seen in Table 7.1. The crack growth parameters used were the ones recommended by Lassen et al. [2005], given in MPa and m;

$$m \quad = 3.0$$

$$\mathsf{C} \quad = 17.5 \cdot 10^{-12}$$

The purpose of the life estimates is to observe the behaviour of the different crack growth hypotheses, and quantify the cumulative difference between them. The effect of crack closure has not been included for these analyses.

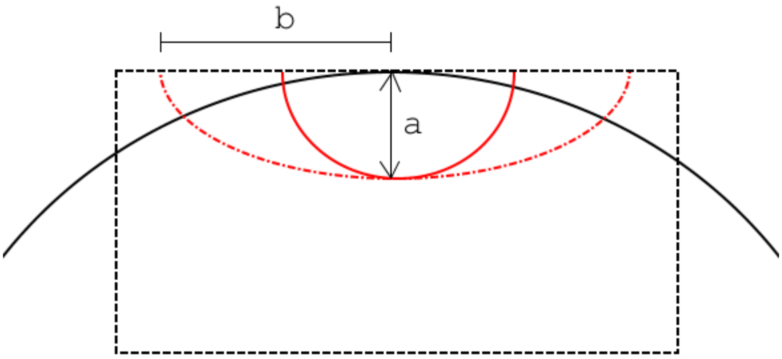

Figure 7.8: Comparison of surface cracks in rod and plate.

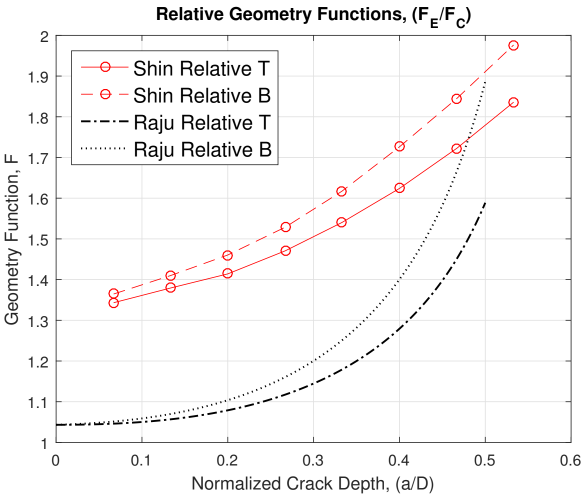

Figure 7.9: Comparison of surface cracks in rod and plate. T is tension and B is bending load.

Table 7.1: Flaw dimensions for the life estimates.

Model	a_i **[mm]**	a_f **[mm]**
Local	0.2	5
Global	5	38
Combined	0.2	38

7.4.1 Local Model

The enclosed crack solution was not included in the local model, but will instead be reviewed with the combined model.

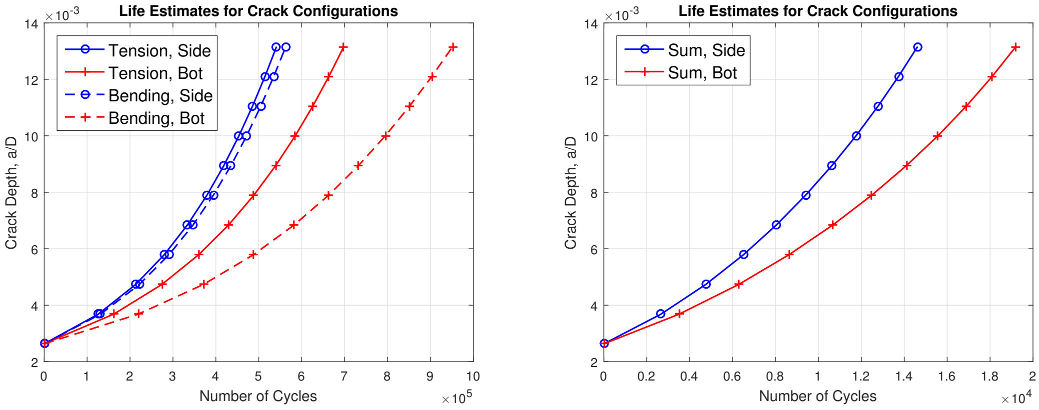

(a) Life estimate with a 100MPa load, on plates. *(b) Life estimate with the equivalent chain load.*

It is seen from Figure 7.10a that the shortest life is to be expected for cracks emitting from the side of the pit, for both types of loading. Therefore, the result is the same when the chain equivalent loading is applied, as seen in Figure 7.10b.

7.4.2 Global Model

The estimated fatigue lives of the chain link when considering only the global model is seen in Figure 7.12. It is easily seen that the assumption of only having a circular crack front gives the largest fatigue life. The fatigue life of a crack starting elliptic and circular is 57% 67%. of the circular only case, respectively. The difference between the crack starting elliptic and circular is not as big as expected, but still not negligible. To simplify analyses later, a constant ratio could be used, but the best fit value for this needs further evaluation.

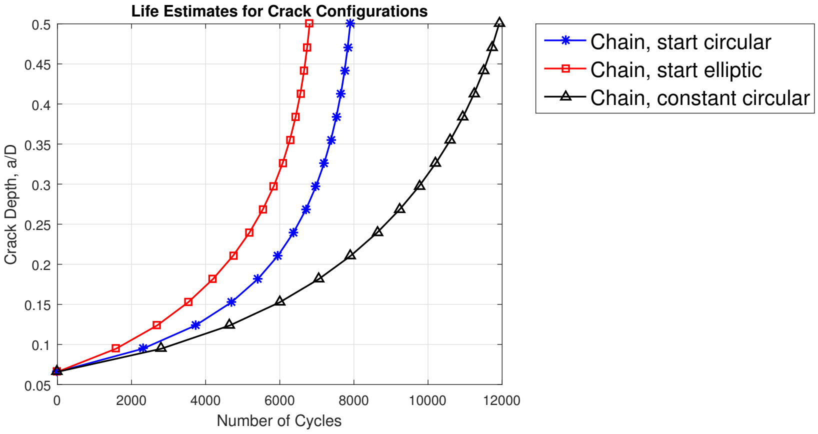

Figure 7.11: Life estimate with a 100MPa load.

7.4.3 Combined Model

For the combined models, the initial crack size was as mentioned set to 0.2. For the hypothesis 3 case, however, the initial crack length was set to 1.2mm. It therefore shows the shortest life, as is to be expected.

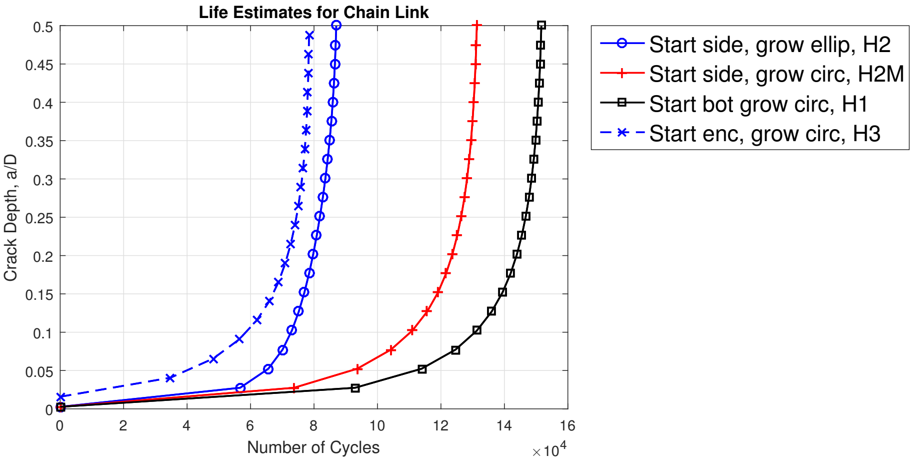

Figure 7.12: Life estimate with a 100MPa load.

The longest life was estimated for hypothesis 2. Table 7.2 gives the lives of the other hypotheses as a percentage of hypothesis 2.

Table 7.2: Relative lives of the different hypotheses.

Hypothesis	Relative Life, [%]
H1	100
H2	57.4
H2M	86.6
H3	51.7

7.4.4 Stress-Life Data

In order to create an SN-curve from the calculated data, the MATLAB program which was used for the life estimation was further developed to allow for varying initial crack length. Lassen et al. [2005] recommends an initial crack depth of 0.12-0.2mm. The current study varies the depth from 0.1 to 0.5mm for all hypotheses, except hypothesis 3, which varies the depth from 1.2 to 1.5mm. The loading levels were approximately the same as are being used in the laboratory experiments at NTNU, and vary from 50 to 100 MPa with a step of 10 MPa. DNV GL's suggested design SN curve for studless links, as seen in Table 3.2, is also included in the plot.

The simulation does not contain any probability aspects, and should therefore be considered as showing only the range of possible outcomes.

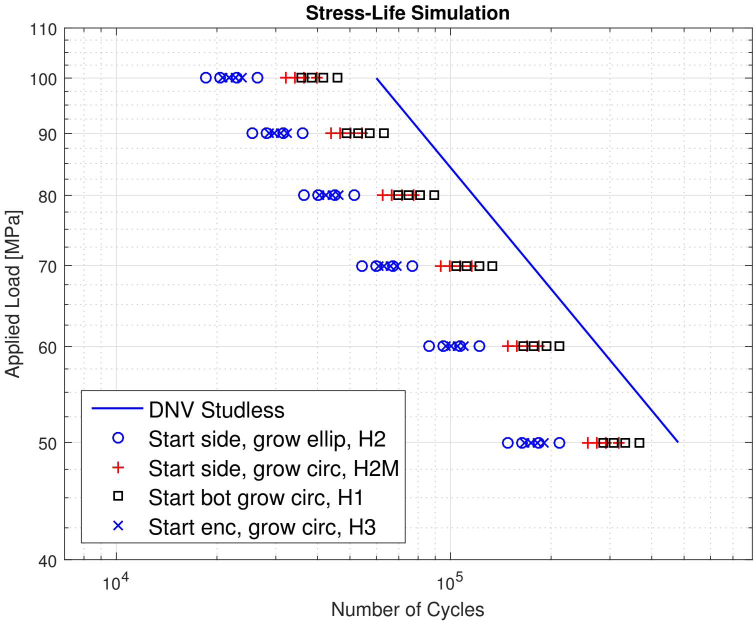

Figure 7.13: SN data generated with varying initial crack depths.

Lassen et al. [2005] recommended the use of a ΔK_{th} of $5MPa\sqrt{m}$ to account for the crack closure effect for corrosion. He states a valid regiment from $10-30MPa\sqrt{m}$. The effect of crack closure was included in Figure 7.14, but is only introduced when ΔK is larger than $10MPa\sqrt{m}$. This was done by finding the depth at which all crack configurations were higher than $10MPa\sqrt{m}$, and then modifying ΔK.

7.4.5 Review of Life Estimates

It is clear from the presented data, that there is a significant difference between the life estimates depending on where the crack initiates. The discrepancy for hypothesis 2 has already been

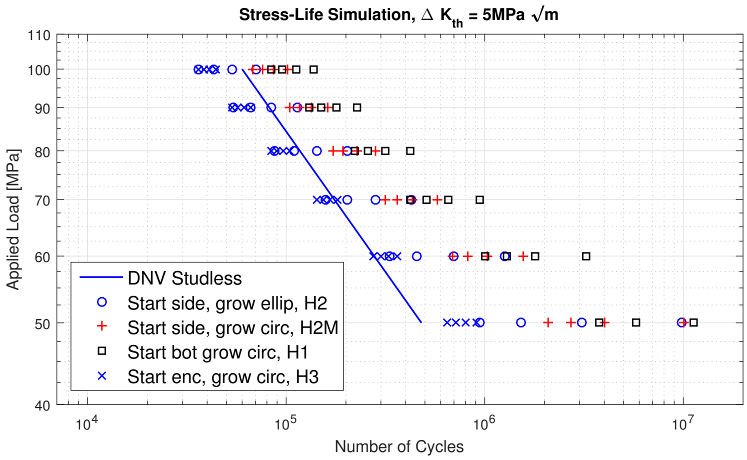

Figure 7.14: SN data generated with varying initial crack depths, and accounting for crack closure.

Table 7.3: Relative portion of life spent in local phase in percentage of total life.

Origin	**Relative Hypothesis**	**% of Total Life**
Bottom	Hypothesis 1 (H1)	24.3
Side	Hypothesis 2 (H2)	53.3
Side	Modified Hypothesis 2 (H2M)	35.3
Enclosed	Hypothesis 3 (H3)	18.3

discussed in Section 7.3. Table 7.3 shows the percentage of the life the crack spends in the local phases of growth, 0.2-5mm for bottom and side cracks, and 1.2-5mm for enclosed crack, compared to the total life of the relevant hypotheses, for the model not including crack closure.

Substantial parts of the lives are spent in the local growth phase for most of the cracks. The enclosed crack has the shortest relative life in the local phase, which is as expected due to it essentially being a fully developed crack, and it starting with a longer crack length. The H2 assumption spends more than half of it's life in the local phase.

The stress life data generated is conservative with respect to the SN-curve, as is to be expected. The fracture mechanics approach does not account for the cycles required for crack initiation, and the chain is modelled as having a corrosion pit in the current analysis. The pit having a detrimental effect on the life is to be expected. The introduction of the crack closure effect substantially increases the expected life of the chain link. It is observed that the spread of the data becomes more pronounced for the lower load levels. This is expected, as the threshold value becomes relatively larger compared to the ΔK from the load as the load decreases.

Chapter 8

Conclusion

The fatigue model tested consisted of two different finite element models, a local and a global model, that were combined by curve fitting their results. The local model simplified the curved surface of the rod as a straight plate with an idealized corrosion pit. Three different hypotheses were made for the crack growth from the pit; the first proposed a circular crack growing from the bottom of the pit transitioning into a circular crack encompassing the pit. The second proposed a crack growing from the side of the pit which would transition into an elliptical crack encompassing the pit. The third proposed the crack initially encompassing the entire pit, and continuing to grow as a circular crack. The local finite element analyses showed that the crack hypotheses tended towards their proposed shapes.

It was found that the crack originating in the side of the pit had the largest stress intensity factor at initiation and throughout it's growth. On this basis and by use of the Kondo criteria for the pit to crack transition, it was suggested that a crack would be more likely to initiate in the side of the idealized pit.

The global model investigated the crack growth through the crown of a chain link. The effect of different crack front ratios throughout the growth was studied. To continue from the initial crack growth hypotheses, the cracks in global model started with an elliptic shape, or a circular shape. Three different propagation models were chosen. Two models, with initial crack ratios of 0.5 and 1.0 varied the ratio as the crack grew through the link according to the analyses performed by Couroneau and Royer [1998]. The third crack had a constant ratio of 1.0 throughout the entire growth. The crack having an initial ratio of 0.5 had the shortest life, followed closely by the crack with an initial ratio of 1.0 with morphing ratio. The crack which remained constant with a ratio of 1.0 throughout the entire growth had a remarkably longer life than the aforementioned cracks. Assuming a crack ratio of 1.0 as was done for the simplified chain link analyses presented in Appendix B is therefore seen as a poor assumption. The simplified chain link analysis methods presented in Appendix B were seen to be non-conservative, in comparison with a three dimensional finite element analyses, and are not recommended for future use, unless the non-conservative property is compensated for with a very conservative crack shape. This could further impact the accuracy however, which is wht is is not recommended.

The local model results were combined with the global model results, by scaling the loading of the local model until it matched the loading in the crown of the chain link. The combined models showed good correlation for the hypotheses 1 and 3. Hypothesis 2 proposed an elliptical crack front at the end of the initial crack growth regime. It was found that the simplification of the surface of the rod as a plate did not hold for elliptical cracks, as the stress intensity factor for an elliptical crack in a rod was substantially higher than for the equivalent crack in a plate. Hypothesis two therefore did not show the expected transitional behaviour.

The results from the local and global model were curve fit to get an estimate for the total crack growth through the crown of the chain link. In order to reduce the error of the hypothesis 2 results, the analyses points from the local model showing values below the corresponding global solutions were removed from the curve fitting.

A MATLAB script was written to integrate Paris' law with the geometry functions of the local, global and combined models. With a load set to 100MPa, the combined model showed life estimates varying from $8 \cdot 10^4$ cycles for the third hypothesis, to $1.45 \cdot 10^5$ cycles for the first hypothesis. The MATLAB script was further developed to generate a series of SN data to show the effect of varying initial crack depth from 0.2 to 0.5mm for the first and second hypothesis, and from 1.2 to 1.5mm for the third. When crack closure was not taken into account, the data set was conservative in comparison with SN curve specified for DNV GL for studless chains. When crack closure was included, the results were consistent with the SN curve from DNV GL, but with a larger scatter due to the crack closure having a larger impact for smaller loads.

Appendix A

Simplified Chain SIF Analysis

As the computational cost of three dimensional SIF analyses are high, two different methods to simplify the calculations were investigated. The first, proposed by Tom Lassen in [Lassen et al., 2005] suggests employing hand book solutions for surface cracks in rods together with a finite element analysis of the stress distribution in the chain, to find the stress intensity factor. The second method, proposed by the author, suggests performing crack analyses on a simplified two dimensional model of the chain, and then correcting the stress intensity factor by using the geometry function for a rod with a surface crack in bending. The methods are summarized in Figure A.1.

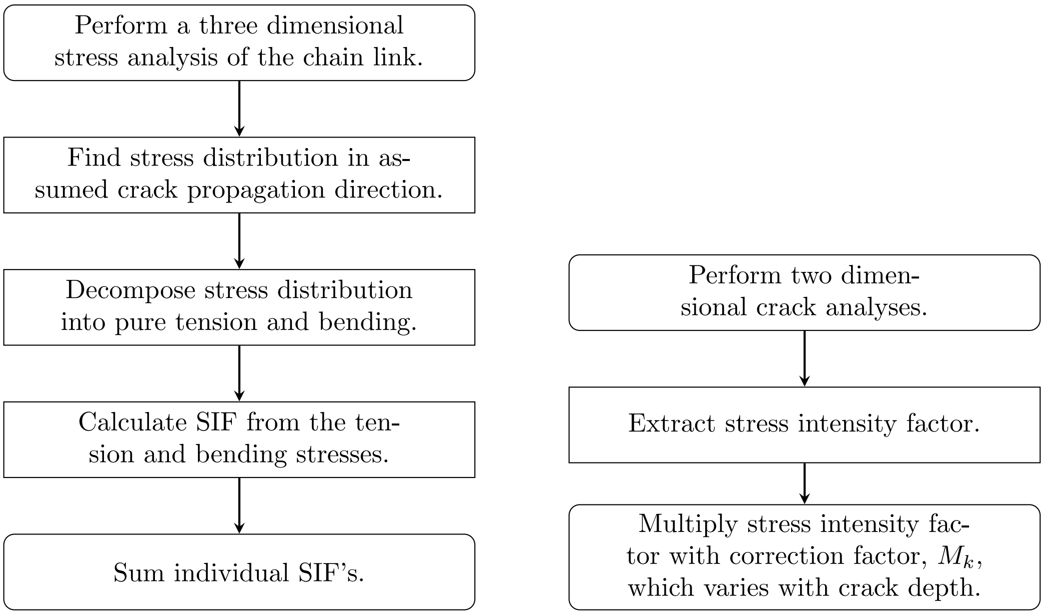

(a) Simplified method based on handbooks.

(b) Simplified method based on two dimensional analyses.

Figure A.1: Flow charts of simplified methods to find SIF for surface crack in chain.

In order to perform the simplified methods, it is readily seen that two analyses are required; a three dimensional stress analysis and a two dimensional crack analysis. The stress analysis with the decomposition of stresses will be introduced first, followed by the two dimensional analysis. In order to verify the results, three dimensional crack analysis were performed with a constant circular crack front. The results from the simplified methods will be compared with these results.

A.1 Three Dimensional Stress Analysis

A.1.1 Model Description

The geometry and boundary conditions applied in the three dimensional analysis are all explained in Section 6. The only difference being the removal of the crack. Also the stress analysis were performed for three different applied surface tractions; 60MPa, 80MPa and 100MPa. The mesh used in the three dimensional analysis is seen in Figure A.2.

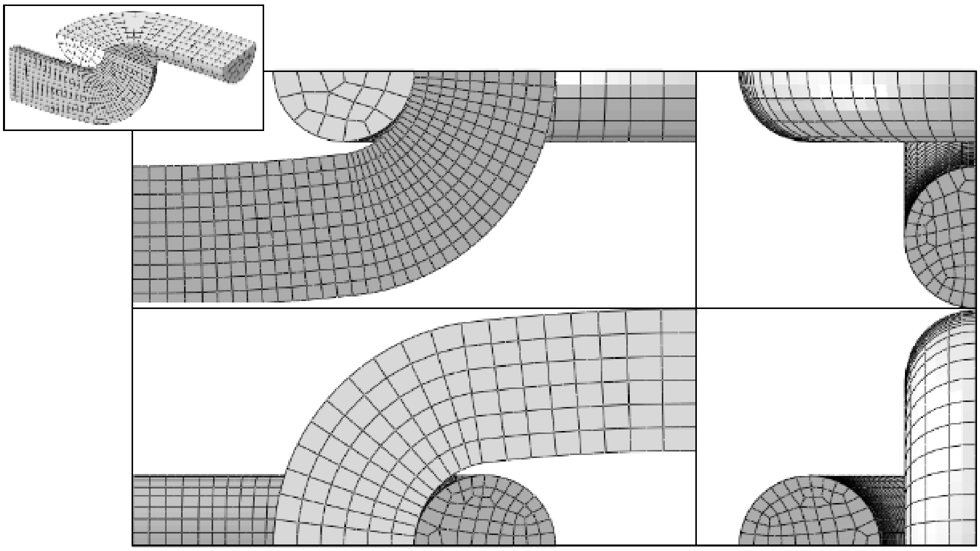

Figure A.2: Geometry, Evy

A.1.2 Results

The resulting stress S11 in the crown, was normalized against the applied surface traction, and the results for the three different load levels are seen in Figure A.3. As is readily seen from the plot, the stresses in the crown are maximum 4.2, C_T, times the applied surface traction, of which the stresses can be decomposed into a pure tension contribution of 0.95, C_t and a pure bending contribution C_b of 3.25 times the applied stress.

A.1.3 Stress Intensity Factor Solutions

Many papers have been published describing the stress intensity factors of different components under tensile and bending loads. Newman and Raju have performed multiple studies where they develop the stress intensity factor for circular and elliptical cracks in plates [Raju and Newman, 1979]and other geometries.

Shin and Cai have performed both experimental and finite element analyses on the stress intenity factors of elliptical surface cracks in rods [Shin and Cai, 2004]. The stress intensity factor is presented as:

$$K_I = F_I \sigma \sqrt{\pi a} \tag{3.22a}$$

Where F_I is presented as tabulated values. The nomenclature used in the tables is described using the Figure A.4.

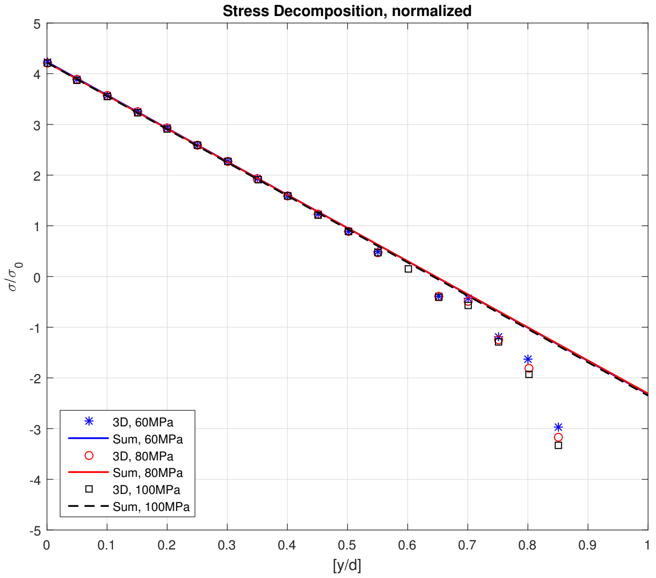

Figure A.3: The decomposed S11 stress in the crown of the chain link.

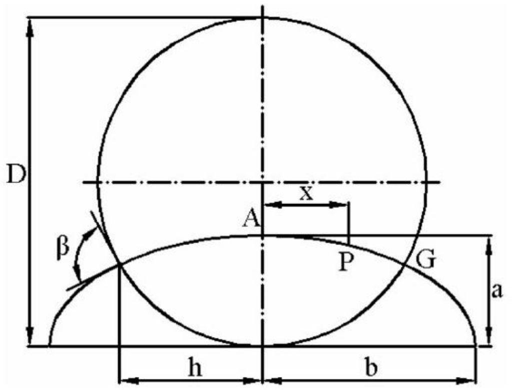

Figure A.4: Description of solution nomenclature, [Shin and Cai, 2004, p.241]

Figure A.5, shows functions fitted by the use of least squares method with third order polynomials to the data points for two different crack ratios.

A.2 Two Dimensional Crack Analysis

A.2.1 Two Dimensional Chain Model

The two dimensional model is a plane strain model with the same general dimensions as the three dimensional model. In order to estimate the crack growth, a total of 38 analyses were performed, starting at a crack depth of 1mm and ending with a crack depth of 38mm.

Geometry

The two dimensional model geometry is equivalent to the profile of a link from the three dimensional model. The contact surface was approximated to be a constant value of 15mm, by

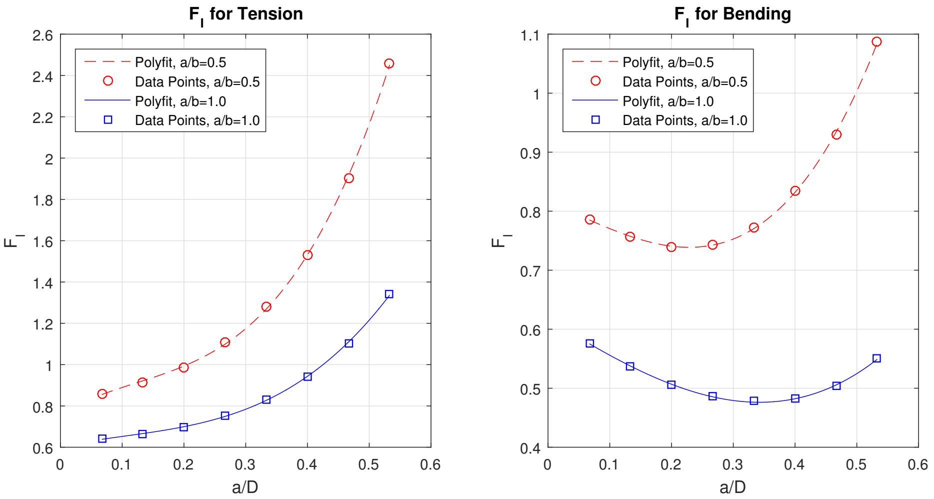

Figure A.5: Description of solution nomenclature, [Shin and Cai, 2004, p.241]

inspecting the contact area in the three dimensional model under different loading conditions.

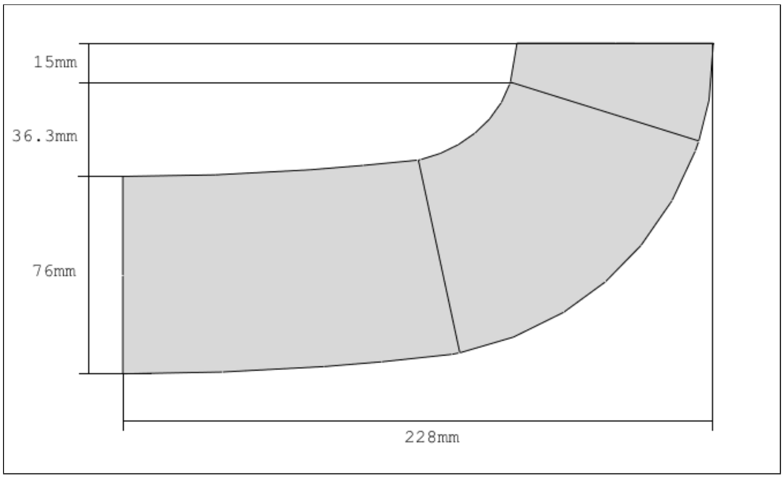

Figure A.6: Geometry, Evy

Mesh

Quadratic second order plane strain elements, CPE8, were used in the simulations. The computational cost of having second order elements is comparatively small, and will give a better stress singularity when performing crack analyses. The second order elements were therefore used for consistency. The mesh is seen in Figure A.7a

Material

The material model is linear elastic, with the same properties as seen in Table 4.1.

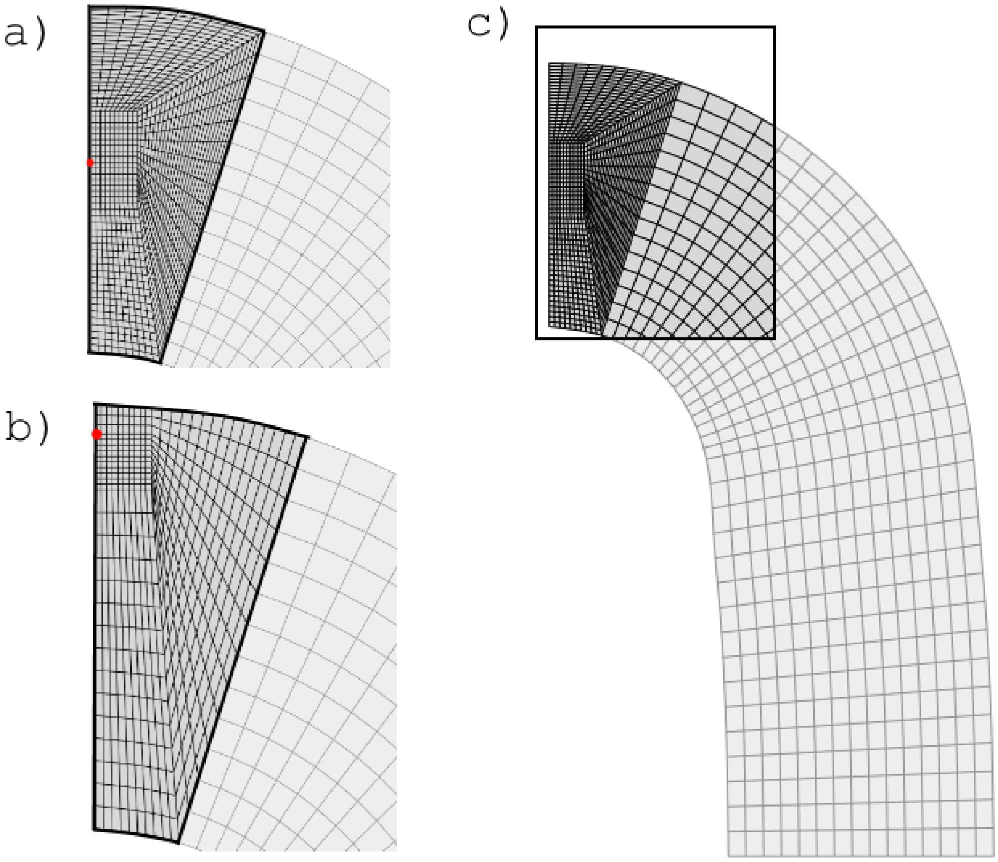

(a) The crack meshes used with the two dimensional model. The red dot indicates the tip of the crack. a) shows the long configuration, while b) shows the close configuartion. c) shows the full mesh with emphasis on the transition region.

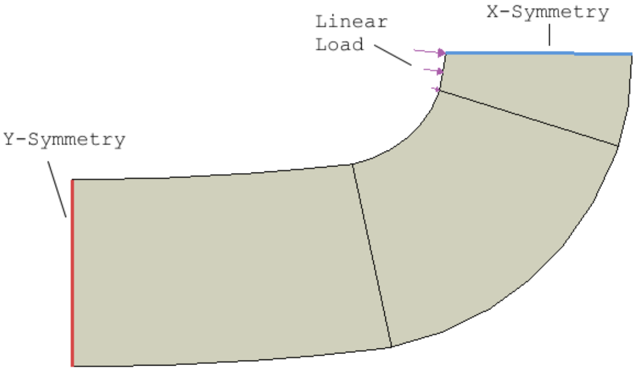

(b) Load, Evy

Boundary Conditions and Loading

The model is symmetric along two axes, Figure A.7b, and is subject to a linear varying pressure load in the crown. The maximum of the load is at the symmetry face in the top of the crown. The load was calibrated through the use of the three dimensional models, by varying the maximum magnitude of the pressure load, until the longitudinal stress in the crown of the two models were similar. It was calibrated against the 100MPa and 60MPa load case for three dimensions, and checked against the 80MPa load. The approximate loading relation used is seen in Eq. 3.22b.

$$q_{max} = 15 + 9.25 \cdot \sigma_0 \tag{3.22b}$$

The linear variance of the load follows Eq. 3.22c, where c_{width} is the width of the contact area, here set as 15mm.

$$q = q_{max} \cdot \left(1 - \frac{y}{c_{width}}\right) \tag{3.22c}$$

Stress Intensity Factor Correction

The SIF correction for the two dimensional case was done by using the handbook solution for a circular crack in a rod for both tension and bending, [Shin and Cai, 2004]. By using the stress linearization to normalize the solution into a combined correction function. As seen in Section A.1.2, the tensile contribution was 0.95, C_t, while the bending contribution, C_b, was 3.25, for a total of 4.2, C_T. By appling Eq. 3.22d, a total correction function was obtained.

$$F_{Tot}(a/D) = \left(\frac{C_t}{C_T}\right) \cdot F_t(a/D) + \left(\frac{C_b}{C_T}\right) \cdot F_b(a/D) \tag{3.22d}$$

The corrected stress intensity factor of the two dimensional chain link thus becomes:

$$K_{I,corr}(a/D) = K_{I,2D}(a/D) \cdot F_{Tot}(a/D) \tag{3.22e}$$

A.3 Three Dimensional Crack Analysis

The reference three dimensional crack analysis were made using the same model as described in Section 6, except that the crack front was constant perfectly circular throughout the whole growth. The crack propagation stages are seen in Figure A.8

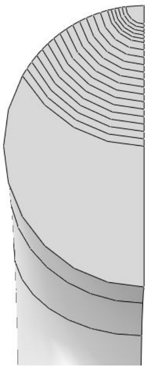

Figure A.8: Crack propagation stages for the three dimensional cracked model. Each circle is one analysis.

A.4 Simplified Analysis Results and Discussion

The results from the simplified analysis are seen in Figure A.9.

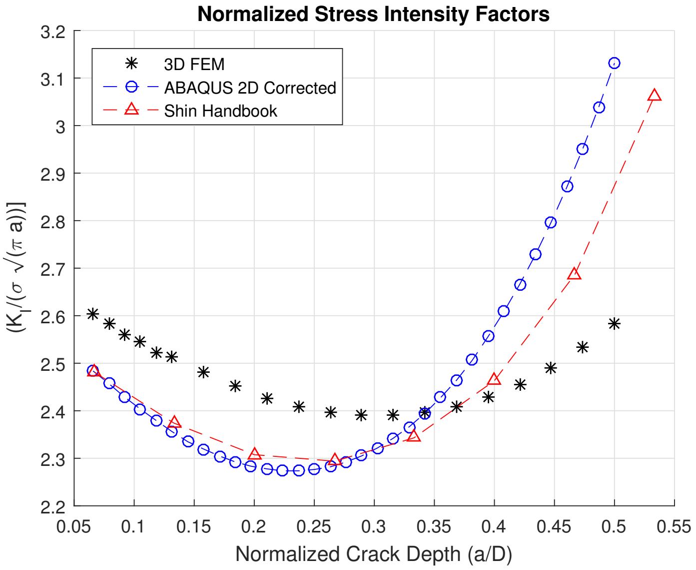

Figure A.9: Normalized SIF results for the simplified and three dimensional analyses.

It is readily seen from Figure A.9, that both the two dimensional chain approach and the handbook solutions show the same trend as the three dimensional analysis.

The data points from the analyses were fit to three different third order polynomial curves through the use of the least squares method. By using these curves, and error estimate of the form Eq. 3.22f was found.

$$E = \frac{(K_{0,3D} - K_{0,simp})}{K_{0,3D}} \tag{3.22f}$$

Where K_0 is the normalized stress intensity factor, and 3D indicates the three dimensional analyses, while simp indicates the respective simplified method.

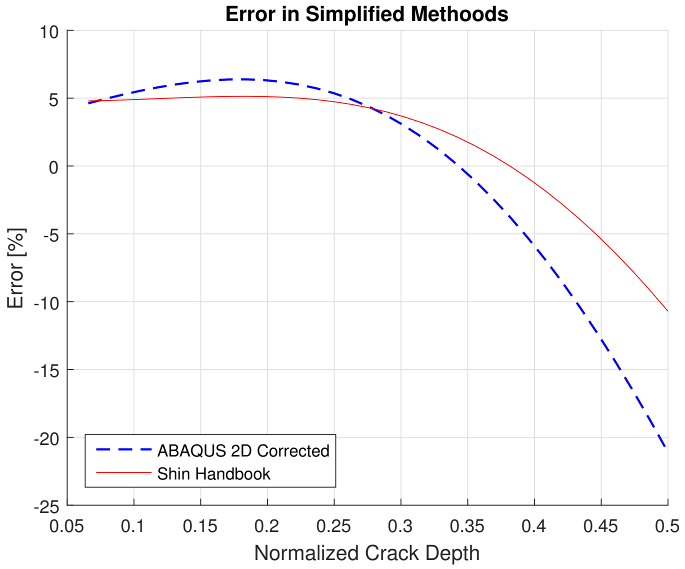

Figure A.10: Error estimate for the simplified SIF analysis methods.

When using simplified fracture mechanic methods for fatigue analyses, the analyst should keep in mind that the early crack growth has a larger impact on the life than the growth towards the end of the life. Thus, it is important with a higher accuracy in the earlier stages. In addition, the methods should be conservative. A non-conservative solution can result in the overestimation of the fatigue life of the component, which can have dire consequences.

In Figure A.10, a conservative error is negative, while a non conservative error is positive. It was expected that the error would be growing for the handbook solutions as the crack propagates, since the stress linearization no longer holds, and the crack moves closer to the highly compressive field which is not represented in the model.

A.5 Conclusion

When applying the aforementioned simplified methods, the analyst should be aware that the solutions show a non conservative trend in the early stages of crack growth, with an error ranging from 5-7%. The proposed simplified method based on two dimensional analyses shows mostly a higher error than the handbook solutions, and the same non conservative properties. The simplified two dimensional analysis method is therefore not recommended for use when estimating the stress intensity factor in the crown of a chain.

Appendix B

Crack Front Shape Development

As was mentioned in Section 3.3.3, the shape of the crack front growing through a rod changes as it propagates. [Couroneau and Royer, 1998] investigates this change in crack front shape, and gives it as a relation between the crack depth, a, and the width of the crack where it intersects the rod, L, as seen in Figure B.1.

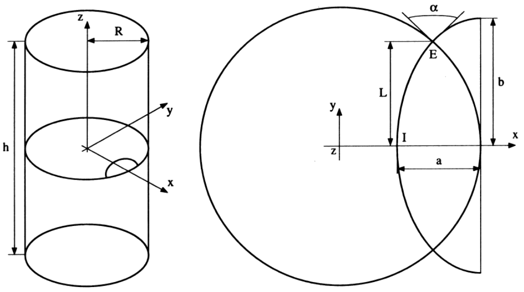

Figure B.1: Stages of crack growth. [Couroneau and Royer, 1998, p.712]

Figure B.2 shows the crack aspect ratio development for bending. It should be noted that the initial crack depth in the plot is (a/R)=0.1.

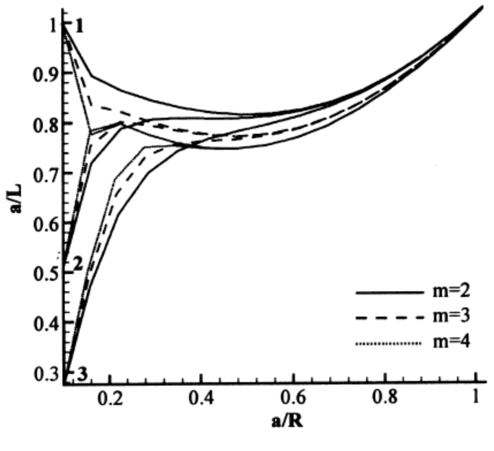

Figure B.2: Changes in aspect ratio with crack growth for bending rod.[Couroneau and Royer, 1998, p.714]

No tabulated data was given in the paper, and it was therefore sampled from the plots, Figure

B.2. The sampled data is seen in Table B.1. Fewer points were sampled for the crack starting as circular, as it showed a clearer trend. The (a/R) values were converted to (a/b), through the use of Eq. 3.22a and later fitted to a third and fourth order polynomial respectively by the least squares method.

$$b = \left(\frac{L^2}{1 - (\frac{R - X_E}{a})^2} \right)^0 .5 \tag{3.22a}$$

The resulting functions for the crack front ratio are:

$$\left(\frac{a}{b} \right)_C = -1.7737 \cdot x^3 + 2.7193 \cdot x^2 - 1.5615 \cdot x + 1.0016 \tag{3.22b}$$

For the crack starting with an (a/b) ratio of 1, and:

$$\left(\frac{a}{b} \right)_E = -5.0470 \cdot x^4 + 14.2546 \cdot x^3 + -11.7320 \cdot x^2 - 3.2707 \cdot x + 0.4967 \tag{3.22c}$$

For the crack starting with an (a/b) ratio of 0.5. The functions are only valid when (a/D) ranges from 0.1 to 0.5, and a crack shorter than this is assumed to have a constant shape.

Table B.1: Data sampled from the plots by Couroneau, all.

(a/b) = 0.5		**(a/b) = 1.0**	
(a/R)	(a/L)	(a/R)	(a/L)
0.10	0.50	0.10	1.0
0.26	0.78	0.26	0.82
0.30	0.80	0.54	0.76
0.40	0.79	0.7	0.8
0.54	0.76	-	-
0.70	0.80	-	-

Appendix C

Curve Fitting

The application Curve Fitting in MATLAB was used for the curve fitting procedures. They were fit to the data points using either polynomials, exponential functions or a combination of the two. The table below contains the names of all the curves used in MATLAB, their reference equation, as well as a description of which data the curve interpolates. Below the table is the script, getFullData, which is called in MATLAB before the integration procedure, containing a selection of the interpolation functions.

Table C.1: Overview of functions generated by curve fitting.

Name	**Region**		**Description**
		Min	Max
Chain_C_E	0.066	0.5	Describes the crack growth from an initially circular crack in the crown of a chain link.
Chain_E_E	0.066	0.5	Describes the crack growth from an initially elliptical crack of ratio (a/b) = 0.5 in the crown of a chain link.
ES_Side	0.0026	0.5	Describes the crack growth from the side of a notch into an elliptical crack in the crown of a chain link.
CS_Side	0.0026	0.5	Describes the crack growth from the side of a notch into a circular crack in the crown of a chain link.
CS_Bot	0.0026	0.5	Describes the crack growth from the bottom of a notch into a circular crack in the crown of a chain link.
CS_Enc	0.0026	0.5	Describes the crack growth from a crack encompassing the notch into a circular crack in the crown of a chain link.

```
global D
% % % PROPAGATION THROUGH CHAIN LINK STARTING FROM CIRCULAR CRACK
p1 =        -255.9;%
p2 =         403.6;%
p3 =        -238.2;%
p4 =         70.98;%
p5 =        -8.758;%
p6 =         2.935;%
Chain_C_E = @(x) p1.*(x/D).^5 + p2.*(x/D).^4 + p3.*(x/D).^3 +...
```

```
    p4.*(x/D).^2 + p5.*(x/D) + p6;


% % % PROPAGATION THROUGH CHAIN LINK STARTING FROM ELLIPTICAL CRACK
p1 =          668.6;%
p2 =          -1073;%
p3 =          652.5;%
p4 =         -168.5;%
p5 =          14.75;%
p6 =          3.063;%
Chain_E_E = @(x) p1.*(x/D).^5 + p2.*(x/D).^4 + p3.*(x/D).^3 +...
    p4.*(x/D).^2 + p5.*(x/D) + p6;



% % % Start growth elliptical, from side
a =         3.918;%
b =           577;%
c =          1.98;%
d =         1.728;%
e =       0.01172;%
f =        -3.185;%
g =        -5.743;%
h =         24.42;%
ES_Side = @(x) a.*exp(-b.*(x/D))+c+d.*exp(e.*(x/D))+...
    f.*(x/D)+g.*(x/D).^2+h.*(x/D).^3;


a =        0.8693;%
b =         26.83;%
c =         2.361;%
d =         1.515;%
e =         2.413;%
f =        -218.6;%
g =        -1.181;%
h =         7.491;%
CS_Side = @(x) a.*exp(-b.*(x/D))+c+d.*(x/D)+...
    e.*exp(f.*(x/D))+g.*(x/D).^2+h.*(x/D).^3;

% % % Start growth circular, from bottom
a =          2.41;%
b =         248.7;%
c =         2.919;%
d =        -8.336;%
e =         67.28;%
f =        -223.6;%
g =           377;%
h =        -237.7;%
CS_Bot = @(x) a.*exp(-b.*(x/D))+c+d.*(x/D)+e.*(x/D).^2+f.*(x/D).^3+...
    g.*(x/D).^4+h.*(x/D).^5;

% % % Start growth circular, from enc
p1 =  -1.516e+05;
p2 =   3.273e+05;
p3 =   -2.92e+05;
```

```
p4 =    1.388e+05;
p5 =   -3.762e+04;
p6 =         5748;
p7 =       -441.7;
p8 =        11.87;
p9 =        2.677;
CS_Enc = @(x) p1.*(x./D).^8 + p2.*(x./D).^7 + p3.*(x./D).^6  +...
     p4.*(x./D).^5 + p5.*(x./D).^4 + p6.*(x./D).^3  +...
     p7.*(x./D).^2 + p8.*(x./D) + p9;
```

Appendix D

Mesh

D.1 Plate Thickness Convergence Study

The test was conducted with a quarter symmetric model, having a circular surface crack, with varying crack depth over plate thickness ratios. The result is seen in Figure D.1.

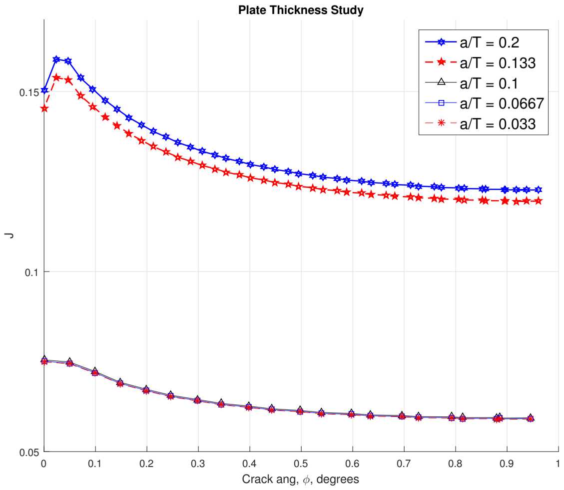

Figure D.1: The convergence of the J-integral with reduced (a/T) ratio.

D.2 Meshing Error

When the midside nodes were moved for the local models, the meshing irregularity as seen in Figure D.2 occurred.

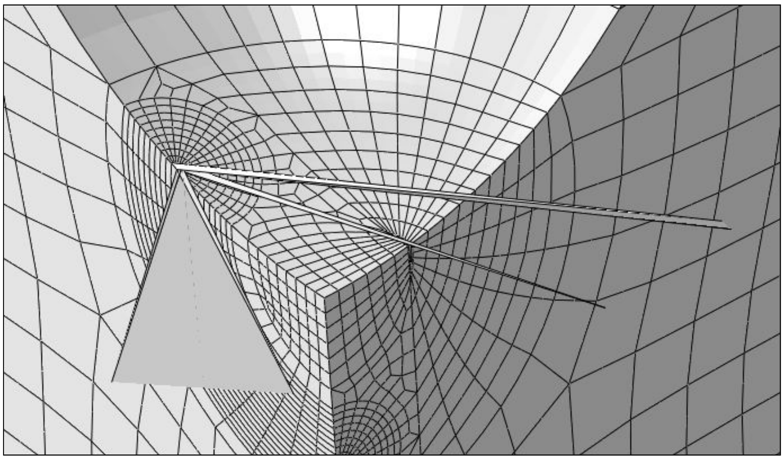

Figure D.2: Meshing irregularity that occured when moving the midside nodes for local model.

Bibliography

Ryan Crighton. Failure of a Flexible Pump Connector. `https://www.energyvoice.com/oilandgas/45369/gryphon-insurance-payouts-close-440m/`. [Online; accessed 10-June-2016].

Leila Keshavarz. Analysis of mooring system for a floating production system. 2011.

Evy Bjørnsen. Chains in mooring systems. 2014.

DNV-OS-H203. Transit and Positioning of Offshore Units. Standard, Det Norske Veritas, February 2012.

Noble Denton Europe. Floating production system - jip fps mooring integrity. 2006.

Alexander Hoel, Kristin Hanem Tømmervåg, and Martin Hove. Assessment of the life of offshore mooring chains. 2015.

Blue Water. `http://www.bluewater.com/products-technology/mooring-systems/subsea-mooring-and-offloading-point-smo`, a. [Online; accessed 03-February-2016].

Blue Water. `http://www.bluewater.com/products-technology/mooring-systems/subsea-mooring-and-offloading-point-smop/internal-turret-mooring-systems/`, b. [Online; accessed 03-February-2016].

Blue Water. `http://www.bluewater.com/products-technology/mooring-systems/subsea-mooring-and-offloading-point-smop/external-turret-mooring-systems/`, c. [Online; accessed 04-February-2016].

Martin G Brown, TD Hall, DG Marr, M English, RO Snell, et al. Floating production mooring integrity jip-key findings. In *Offshore Technology Conference*. Offshore Technology Conference, 2005.

SubsTech. `http://www.substech.com/dokuwiki/doku.php?id=resistance_welding_rw`. [Online; accessed 03-March-2016].

Ramnäs. Ramnäs Technical Brochure.

DNV-OS-E302. Offshore Mooring Chain. Standard, Det Norske Veritas, October 2008.

DNV-OS-E301. Position Mooring. Standard, Det Norske Veritas, October 2013.

Isabel Ridge, Philip Smedley, and Roger Hobbs. Effects of twist on chain strength and fatigue performance: small scale test results. In *ASME 2011 30th International Conference on Ocean, Offshore and Arctic Engineering*, pages 183–189. American Society of Mechanical Engineers, 2011.

Kai-tung Ma, Hongbo Shu, Philip Smedley, Didier L'Hostis, Arun Duggal, et al. A historical review on integrity issues of permanent mooring systems. In *Offshore Technology Conference*. Offshore Technology Conference, 2013.

P Jean, K Goessens, D L'Hostis, et al. Failure of chains by bending on deepwater mooring systems. In *Offshore Technology Conference*. Offshore Technology Conference, 2005.

Walter Schütz. A history of fatigue. *Engineering fracture mechanics*, 54(2):263–300, 1996.

Norman E Dowling. *Mechanical Behavior of Materials: Engineering methods for Deformation, Fracture, and Fatigue.* Fourth edition.

ASME International. Failure of a Flexible Pump Connector. `http://products.asminternational.org/fach/data/fullDisplay.do?database=faco&record=1029&search=`, a. [Online; accessed 03-March-2016].

Gunnar Härkegård. Lecture 1 Material. Fatigue Design Course TMM4195, 2015.

ASME International. Fatigue Crack Propagation. `http://www.asminternational.org/emails/enews/amp_pdfs/amp16605p039.pdf`, b. [Online; accessed 03-March-2016].

Sigmund Ås. Fatigue life prediction of an aluminium alloy automotive component using finite element analysis of surface topography. 2006.

Y Kondo. Prediction of fatigue crack initiation life based on pit growth. *Corrosion*, 45(1):7–11, 1989.

Robert P Wei. Material aging and reliability of engineered systems. In *Environmentally Assisted Cracking: Predictive Methods for Risk Assessment and Evaluation of Materials, Equipment, and Structures.* ASTM International, 2000.

Xin-Yan Zhang, Shu-Xin Li, and Rui Liang. Effect of corrosion pits on fatigue life and crack initiation. In *ICF13*, 2013.

DNV-RP-C203. Fatigue Design of Offshore Steel Structures. Standard, Det Norske Veritas Germanischer Lloyd, June 2014.

William N Sharpe. *Springer handbook of experimental solid mechanics.* Springer Science & Business Media, 2008.

George E Totten. *Handbook of residual stress and deformation of steel.* ASM international, 2002.

Charles Edward Inglis. Stresses in a plate due to the presence of cracks and sharp corners. *Spie Milestone series MS*, 137:3–17, 1997.

T. L. Anderson. *Fracture Mechanics, Fundamentals and Applications.* Taylor Francis Group, third edition, 2007.

IS Raju and JC Newman. Stress-intensity factors for a wide range of semi-elliptical surface cracks in finite-thickness plates. *Engineering Fracture Mechanics*, 11(4):817–829, 1979.

CS Shin and CQ Cai. Experimental and finite element analyses on stress intensity factors of an elliptical surface crack in a circular shaft under tension and bending. *International Journal of Fracture*, 129(3):239–264, 2004.

James R Rice. A path independent integral and the approximate analysis of strain concentration by notches and cracks. *Journal of applied mechanics*, 35(2):379–386, 1968.

PC Paris and Fazil Erdogan. A critical analysis of crack propagation laws. *Journal of basic engineering*, 85(4):528–533, 1963.

Mf Klesnil and P Lukáš. Influence of strength and stress history on growth and stabilisation of fatigue cracks. *Engineering Fracture Mechanics*, 4(1):77–92, 1972.

Fredrik Øgård Sirevaag. Modeling of fatigue from random corrosion pits. 2015.

XB Lin and RA Smith. An improved numerical technique for simulating the growth of planar fatigue cracks. *Fatigue & Fracture of Engineering Materials & Structures*, 20(10):1363–1373, 1997.

N Couroneau and J Royer. Simplified model for the fatigue growth analysis of surface cracks in round bars under mode i. *International Journal of Fatigue*, 20(10):711–718, 1998.

J Toribio, JC Matos, B González, and J Escuadra. Numerical modelling of crack shape evolution for surface flaws in round bars under tensile loading. *Engineering Failure Analysis*, 16(2):618–630, 2009.

BS7910:2013. Guide to methods for assessing the acceptability of flaws in metallic structures. Standard, British Standard Institute, December 2013.

Jonathan Fernández, Walther Storesund, and Jesús Navas. Fatigue performance of grade r4 and r5 mooring chains in seawater. In *ASME 2014 33rd International Conference on Ocean, Offshore and Arctic Engineering*, pages V01AT01A035–V01AT01A035. American Society of Mechanical Engineers, 2014.

Tom Lassen, Eirik Storvoll, and Arild Bech. Fatigue life prediction of mooring chains subjected to tension and out of plane bending. In *ASME 2009 28th International Conference on Ocean, Offshore and Arctic Engineering*, pages 229–239. American Society of Mechanical Engineers, 2009.

Tom Lassen, Jose L Arana, Jan Henriksen, Nina K Holthe, et al. Crack growth in high strength chain steel subjected to fatigue loading in a corrosive environment. In *ASME 2005 24th International Conference on Offshore Mechanics and Arctic Engineering*, pages 93–101. American Society of Mechanical Engineers, 2005.

Yordan Garbatov, C Guedes Soares, and Joško Parunov. Fatigue strength experiments of corroded small scale steel specimens. *International journal of fatigue*, 59:137–144, 2014.

JC Newman and IS Raju. An empirical stress-intensity factor equation for the surface crack. *Engineering Fracture Mechanics*, 15(1-2):185–192, 1981.